Non-Linear Time Series Analysis Methods and Their Application to Fluctuation Data From Plasma Experiments

by

Aparajit Gnanasekaran

A thesis submitted in partial fulfillment of the requirements for the degree of

Master of Science

Department of Physics
University of Alberta

Abstract

Non-linear fluctuations are a common feature of data extracted from plasma experiments and are common in the edge regions of magnetically confined plasmas where long filament-like structures of density and temperature can generate them. These fluctuations are associated with turbulence and vortices leading to complex chaotic transport in these regions. Hence, the analysis of these fluctuations are important due to the applications of plasma confinement in research like nuclear fusion.

Non-linear time series are present in many fields of research such as atmospheric sciences, neuroscience, finance, seismology and more. Hence, methods to understand non-linear dynamics has been of utmost importance to researchers. One of the main outcomes of non-linear time series analysis is to identify the nature of the time series as periodic, chaotic or stochastic. There have been many methods developed to perform this analysis from well established methods such as Lyapunov exponents to newly developed methods such as multifractal analysis.

The following thesis explores three methods of non-linear time series analysis: CH-Plane method, Hurst exponent and Lyapunov exponent. CH-Plane is a newly developed method to identify whether a time series is based on underlying dynamics of a deterministic or stochastic nature. Hurst exponent is a well known quantifier for the memory of a system. Lyapunov exponent is the most commonly used quantifier for the degree of chaotic nature in a system. These methods are used to analyze Ion Saturation Current and Floating Voltage fluctuation data from a plasma experiment focusing on cross-field transport fluctuations associated with temperature filaments in cold plasma background. Through this, the thesis shows the breadth of non-linear time series analysis methods available to researchers and their applications in plasma research.

This thesis is dedicated to my family and friends for

supporting me throughout my degree

Acknowledgements

Table of Contents

List of Figures

CHAPTER 1.

INTRODUCTION

Plasmas are very common in the universe from space plasmas such as those that make up stars to atmospheric plasmas such as the auroras to even closer on Earth in devices such as neon lights and welding arcs. Study of plasmas then becomes a very important means to understanding our own universe. To achieve this, plasmas have been created in labs on Earth and held in magnetic containment devices such as tokamaks. The foremost application of such lab plasmas in recent times has been in nuclear fusion experiments as they are the best medium to facilitate fusion as evidenced by the very stars in our universe. This results in a need to understand the behaviour of magnetized plasmas and as well as their interactions with the containment fields at the edges of the system. In this direction, this thesis puts forth the analysis performed on data collected from experiments exploring one behaviour of magnetized plasmas: particle and energy transport through fluctuations from filamentary structures in plasma.

Any discussion regarding plasma must begin with defining plasma. Plasma is an ionized gas that exhibits quasi-neutrality and collective behaviour[1]. The collective behaviour refers to the fact that particles in a plasma exhibit similar behaviour and move together like a fluid[1]. As plasmas are made of charged particles, there are electromagnetic forces that tie their behaviour together. Quasi-neutrality refers to the fact that the density of the various charged particles can be considered to be nearly equal and hence they can all be treated to have a single plasma density[1].

However, since it is an ionized gas, it must be kept confined by a strong magnetic field. For an ionized gas to be considered a plasma, it has to satisfy three conditions. First, the length of the system must be greater than the electron Debye length, λ_d:

$$\lambda_{de} = \sqrt{\frac{\epsilon_o k T_e}{ne^2}} \tag{1.1}$$

Second, the number of particles in the Debye sphere must be much greater than one. Thirdly, the product of the plasma frequency, ω, and the mean time between collisions, τ, must be greater than one[1]. Plasmas are generally characterized by two properties: the number density, n, and temperature, generally written with the Boltzmann constant k as kT, of the charged particles making up the plasma[1]. The vast range of particle densities and temperatures leads to the existence of a great variety of plasmas from space plasmas to gas discharges. Of great interest among these types of plasmas is particle transport and energy transport. This thesis explores the transport and fluctuations from filament-like structures in plasma.

Transport is a characteristic phenomena of magnetically confined plasma with a pressure gradient[2]. Pressure gradients can be generated by structures in plasma such as temperature filaments. Transport in plasmas appears in two forms: diffusion of particles through the plasma known as particle transport and the transfer of energy through the plasma known as heat transport. Local transport for ambipolar diffusion is modelled by Fick's law[1] which defines particle flux and heat flux respectively as:

$$\Gamma_e = \left(D_e{}^{Classical} + D_e{}^{Anomalous}\right)\nabla n_e \tag{1.2}$$

$$Q_e = \left(\chi_e{}^{Classical} + \chi_e{}^{Anomalous}\right)\nabla T_e \tag{1.3}$$

Here, D_e and χ_e are the electron particle and thermal diffusivity respectively and

consist of a classical component and anomalous component. Classical transport is determined through collisional mechanisms while the anomalous transport is made of many forms of cross-field waves and oscillations[1]. Transport in plasma is driven by fluctuations in temperature and density. Fluctuations are a common feature of any magnetized plasma[3].

$$D_e{}^{Anomalous} = \frac{\langle \tilde{n}_e \tilde{v}_r \rangle}{\nabla n_e} \tag{1.4}$$

$$\chi_e{}^{Anomalous} = \frac{\langle \tilde{T}_e \tilde{v}_r \rangle}{\nabla T_e} \tag{1.5}$$

Here, $\tilde{n}_e$ is the fluctuation in electron density, $\tilde{T}_e$ is the fluctuation in electron temperature and $\tilde{v}_r$ is the fluctuation in radial velocity. The transport then depends on the fluctuations of the plasma parameters and drift velocity of the electrons. Fluctuation of the plasma parameters depend on potential fluctuations when the velocity is mainly dominated by $E \times B$ drift.

Collisional transport is the classical transport mechanism where heat is transported through collisions between the ions and electrons. The classical transport from a heat source like a temperature filament is done through thermal diffusion along both the axial and radial directions controlled by the thermal conductivity in those respective directions. So, in a magnetically confined plasma with magnetic field $B_o \hat{z}$, the electron thermal conductivity is[4]:

$$\kappa_\parallel = \frac{(3.16) n_e T_e \tau_e}{m_e} \tag{1.6}$$

$$\kappa_\perp = 1.47 \frac{\kappa_\parallel}{(\Omega_e \tau_e)^2} \tag{1.7}$$

Here $\kappa_\parallel$ is the thermal conductivity along the magnetic field while $\kappa_\perp$ is the thermal conductivity perpendicular to the magnetic field. n_e, T_e and m_e are the electron

density, electron temperature and electron mass respectively. Finally, τ_e is the electron collision time of the plasma, Ω_e is the electron cyclotron frequency and Λ is the coulomb logarithm which are defined as:

$$\tau_e = \frac{(3.44 \times 10^5)T_e^{3/2}}{n_e\Lambda} \tag{1.8}$$

$$\Omega_e = \frac{eB_o}{m} \tag{1.9}$$

$$\Lambda = 12\pi n\lambda_d^3 \tag{1.10}$$

From the above equations, it can be seen that transport along the magnetic field, $\kappa_\parallel \propto T_e^{5/2}$, is much higher than perpendicular to the magnetic field, $\kappa_\perp \propto T_e^{-1/2}$, leading to classical transport being anisotropic[4]. The transport equation for collisional transport in two dimensions in cylindrical co-ordinates can then be written as[4]:

$$\frac{3}{2}n\partial_t T_e = \frac{1}{r}\partial_r\left(r\kappa_\perp\partial_r T_e\right) + \partial_z\left(\kappa_\parallel\partial_z T_e\right) - 3\frac{m_e n}{m_i\tau_e}\left(T_e - T_i\right) + Q \tag{1.11}$$

Here, Q is the total heat in the plasma system from the external heat source. T_i and m_i are the ion temperatures and ion masses respectively.

Anomalous transport is generated by unstable waves in non-equilibrium plasmas with macroscopic gradients in density and/or temperature. A common type of anomalous transport to be focused on in this thesis are resistive drift waves in magnetically confined plasmas. Resistive drift waves are a type of pressure gradient driven universal instability[1]. They resemble a twisted flute and have a rotation around the magnetic field direction as they propagate slowly along the magnetic field direction as seen in fig.1.1a. For a magnetically confined plasma in a magnetic field $B_o\hat{z}$, the

(a) Flute Instability   (b) Drift Wave
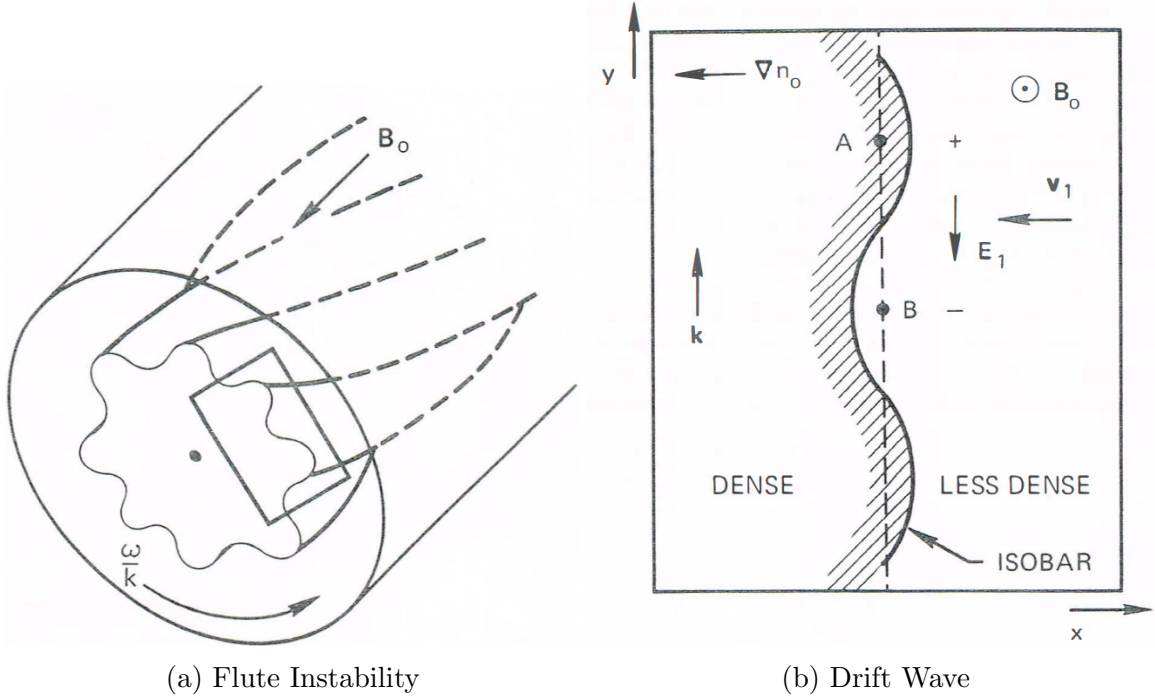
Figure 1.1: The schematic of a resistive drift wave is shown. The left panel shows the propagation of the drift wave through a plasma column. The right panel shows the density fluctuations of the drift wave. The figures are taken from the textbook "Introduction to Plasma Physics and Controlled Fusion" by Chen[1].

drift of the ions and electrons under a density gradient of $KT\nabla n_o$, respectively is[1]:

$$v_i = \frac{KT_i}{eB_o}\frac{n_o{}'}{n_o}\hat{y} \tag{1.12}$$

$$v_e = -\frac{KT_e}{eB_o}\frac{n_o{}'}{n_o}\hat{y} \tag{1.13}$$

Further, the electrons flow along the magnetic field with the drift waves establishing a thermodynamic equilibrium resulting in them now obeying a Boltzmann relation[1]:

$$\frac{n_1}{n_o} = \frac{e\phi_1}{KT_e} \tag{1.14}$$

Due to the above pressure gradient, a density variation is created between the region

within the instability with higher density n_1 and outside with lower density n_0 as seen in fig.1.1b[1]. This creates an electric field, E_1 from the denser region inside to the rarer region outside causing a drift velocity v_1 in the x-direction[1]:

$$v_{1x} = \frac{E_y}{B_o} = \frac{ik_y\phi_1}{B_o} \tag{1.15}$$

Assuming that the fluctuations are incompressible in the x-direction and that the wave propagates faster across the field rather than along, the equation of continuity is[1]:

$$\frac{\partial n_1}{\partial t} = -v_{1x}\frac{\partial n_o}{\partial x} \tag{1.16}$$

Putting in Eqn.1.14 and Eqn.1.15 into Eqn.1.16 , we get[1]:

$$\frac{ik_y\phi_1}{B_o}n_o{}' = -i\omega\frac{e\phi_1}{KT_e}n_o \tag{1.17}$$

$$\Rightarrow \frac{\omega}{k_y} = -\frac{KT_e}{eB_o}\frac{n_o{}'}{n_o} = v_e \tag{1.18}$$

This is the electron drift velocity defined in eqn.1.13. Since these waves move at electron drift velocities, they are called drift waves. Moreover, electron-ion collisions act as a resistance causing a potential drop between the crest and trough of a wave stopping the electric field from the electron flow along the magnetic field from growing indefinitely[1]. This additional effect results in these waves being called resistive drift waves. The dispersion relation for resistive drift waves is[1]:

$$\omega^2 + i\sigma_\parallel(\omega - \omega_o) = 0 \tag{1.19}$$

$$\omega_o = k_y v_e \tag{1.20}$$

If $\sigma_\parallel \gg \omega$, then, the dispersion relation can only be satisfied if $\omega \approx \omega_o$. Then, the dispersion relation can be written as[1]:

$$\omega \approx \omega_o + (i\omega_o{}^2/\sigma_\parallel) \tag{1.21}$$

From the dispersion relation, it can be clearly seen that the drift waves have a positive imaginary part for the frequency making them unstable. The transport equation for temperature in the presence of these drift waves in two dimensions is[5]:

$$\frac{3}{2}n(\partial_t T_e + v_x \partial_x T_e + v_y \partial_y T_e) = \partial_x(\kappa_\perp \partial_x T_e) + \partial_y(\kappa_\perp \partial_y T_e) - \kappa_\parallel \frac{T_e}{L^2} + Q_{ei} + Q_{eff} \tag{1.22}$$

Q_{eff} is the radial heat flux from the filament and Q_{ei} is the heat loss from electron-ion collisions while L is the characteristic length of the temperature filament. To solve this transport equation, a model of the drift velocity, $\{v_x, v_y\}$ is needed which depends on potential fluctuations as[5]:

$$\vec{v_d} = -(c/B)\nabla_\perp \Phi \times \hat{z} \tag{1.23}$$

Hence, to study the fluctuations, a model of potential is sufficient as everything else is governed by it. It has been found from previous experiments that drift waves start with an azimuthal mode of m=1 before evolving to higher order modes. The plasma experiment under analysis is dominated by drift waves with mode m = 1 and a global mode or m = 0 mode[5]. There is also a smaller contribution from a higher m = 6 mode. This potential was modeled by Shi et al. as[5]:

$$\Phi(r, \theta, t) = Re\left[A_1 J_1(k_1 r)e^{i\theta}e^{-i\omega t}e^{-\alpha r} + A_6 J_6(k_6 r)e^{i6\theta}e^{-i\omega t}e^{-\alpha r}\right] + Akr^2 \tag{1.24}$$

Here, r and θ are the radial and angular distances away from the center of the filament and t is the time. k, k_1 and k_6 are the wave numbers of the global mode, the first mode and the sixth mode of the oscillation while A, A_1 and A_6 are the amplitudes of the respective modes. ω is the frequency of oscillation and α represents the temperature gradient around the filament.

Finally, as the drift waves die down, the fluctuations become chaotic in nature and transport is governed by these chaotic fluctuations as long as the heat source remains[5]. Drift waves and chaotic fluctuations will inevitably occur in any plasma with a pressure gradient such as magnetically confined plasma. This results in a need to understand these waves in depth to improve the performance of the confinement devices. However, these fluctuations are non-linear in nature. Hence, to analyze the data from plasma experiments, methods to analyze non-linear time series are needed.

(a) M1 + M0   (b) M1 + M6 + M0
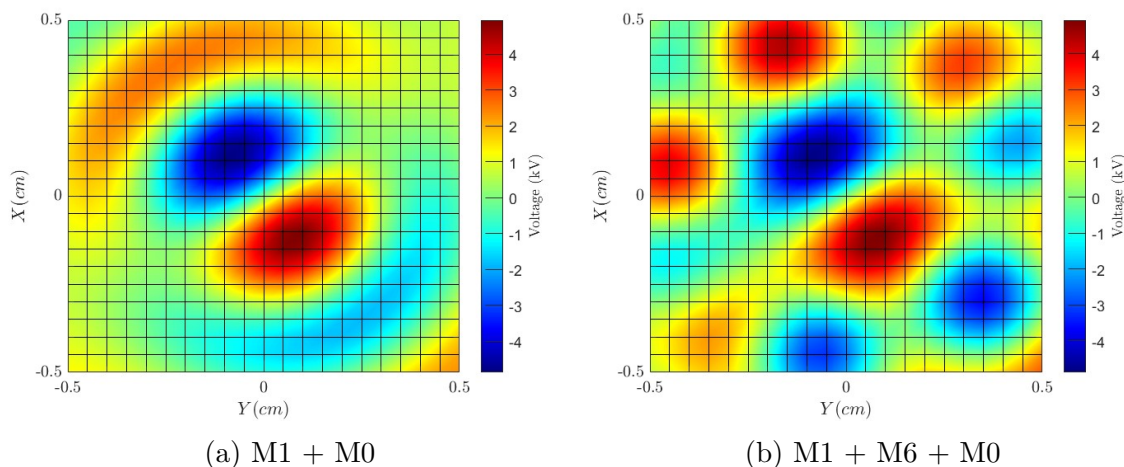
Figure 1.2: Shi-Pace model potential is plotted for various modes of drift waves. The left panel shows the drift wave with mode 1 visible at the centre and the global mode visible at the outer edges. The right panel shows the drift wave with mode 1 visible at the centre, mode 6 visible at the outer edges and the global mode.

It has been shown by Wold that any stationary time series can be defined as a

sum of a deterministic time series and a stochastic time series[6]. The deterministic part of a time series can be periodic or chaotic. Hence, identifying the nature of a time series is an important avenue of analysis for experimental data.

A periodic system is one of the most basic systems seen in nature from pendulums to harmonic oscillators. A periodic system is a deterministic system defined by a set of equations, differential or otherwise, consisting of periodically varying coefficients[7]. A periodic system, $X(t)$ is defined by its time period, T, which defines how long it takes before the system reaches the previously recorded state, i.e, $X(t+T) = X(t)$[7]. The most common form of a periodic systems are trigonometric functions describing circular motion.

Chaotic systems are very commonly observed from natural systems such as weather patterns to man-made systems such as stock markets[8]. Chaotic systems are deterministic systems that are modelled by simple set of differential equations and show complicated behaviour[9]. Their major identifying feature is their sensitivity to initial conditions. So, for two particles in a chaotic system separated by an initial distance δx, the separation after some time t is $\delta x e^{\lambda t}$[8], where λ is the Lyapunov exponent. Essentially, any perturbation in the initial conditions of the system is enhanced exponentially up to saturation as the system evolves. Chaotic systems are appealing as their extremely irregular behaviour is controlled by very simple differential equations. Hence, many mathematical methods such as multifractal analysis, attractor reconstruction and more have been devised that allow researchers to take chaotic time series recorded from a system in an experiment and reconstruct the differential equation that define the system[9]. Hence, identifying chaotic nature in experimental data is extremely useful as it allows the system under study to be analyzed through simple mathematical tools.

Stochastic processes are a common description of complex random process taking

place in nature. A very well known example is the random motion of particles in a gas called Brownian Motion. Stochastic processes are time series of random variables resulting from functions depending on a single index of values such as time or real numbers[10]. Due to their random nature, the future behaviour of stochastic series cannot be determined based on its previous behaviour unlike chaotic series. Due to this, stochastic series are analyzed through their statistics instead. The random variables making up the stochastic series are studied based on their probability distributions and state space[10].

Both chaotic and stochastic series can show strong non-linearity and unpredictability making distinguishing them using linear analysis like Fourier transforms difficult[11–13]. Further, chaotic series derived from higher-dimensional non-linear process share a lot of properties with stochastic series such as wide-band power spectrum[13, 14]. Low-dimensional chaos is even harder to distinguish from stochastic processes in experimental data[12, 15–17]. While chaotic systems can be described through simple equations and stochastic nature can be studied through statistics, identifying such nature in a time series is difficult. Complex systems show strong non-linearity due to the presence of a lot of microscopic sub-systems varying on fast time scales that interact non-linearly with collective behaviour of the system varying on longer time scales[10]. So, any time series recorded from such complex systems in experiments is consequently going to be non-linear in nature.

A time series is generally seen as a realization from a stochastic process. For a finite set of time indexed data, there are infinitely many stochastic processes that can be considered to model the data. Finding the best model out of the infinite possibilities to characterize the underlying process is one of the main goals of time series analysis. A linear time series is one which is recorded from a linear process

which is a process that obeys superposition and scaling properties as follows[18]:

$$f(ax + by) = af(x) + bf(y); \ a, b \in R \tag{1.25}$$

where a and b are the scaling factors. A linear time series is usually modelled using ARMA models made of an auto-regressive (AR) model and a moving average (MA) model[19]. An auto-regressive model of a time series, X, describes the time series as a linear regression model made of its past values. An AR model of the time series X of order p is then defined as[19]:

$$X(t) = b_1 X(t-1) + b_2 X(t-2) + ... + b_p X(t-p) + \epsilon \tag{1.26}$$

Here, ϵ is white noise. A moving average model on the other hand defines a linear time series as a moving average of white noise of order q as[19]:

$$X(t) = \epsilon(t) + a_1 \epsilon(t-1) + a_2 \epsilon(t-2) + ... + a_q \epsilon(t-q) \tag{1.27}$$

These two models are combined to give the ARMA model of order (p, q) used to define linear time series[19]:

$$X(t) = b_1 X(t-1) + b_2 X(t-2) + ... + b_p X(t-p)+ \tag{1.28}$$

$$\epsilon(t) + a_1 \epsilon(t-1) + a_2 \epsilon(t-2) + ... + a_q \epsilon(t-q) \tag{1.29}$$

However, over the years, many time series have been identified in experiments that cannot be modelled through models used for linear time series. These time series are referred to as non-linear time series. Such time series are characterized by features such as non-normality, asymmetric cycles, sensitivity to initial conditions and

more[19]. These features make analysis of non-linear time series difficult as linear models cannot adequately represent the non-linear features resulting in the need for purpose built tools to analyze non-linear time series. This thesis focuses on three such tools: CH-Plane method, Hurst exponent and Lyapunov exponent.

The CH Plane is a method to analyze a given time series to see if it is periodic, chaotic or stochastic by plotting the entropy of the series against its complexity. This method is the focus of Chapter 2. Hurst exponent is a quantitative measure of memory of a system and is focused on in Chapter 3. Lyapunov exponent is a very commonly used measure based on particle trajectories to quantify the degree of chaotic nature of a time series and is focused on in Chapter 4. Further, machine learning is used to relate Hurst and Lyapunov exponents. The three methods are used to analyze fluctuation time series data from a plasma experiment to show the application of non-linear time series analysis.

CHAPTER 2.

ENTROPY-COMPLEXITY PLANE

Analysis of time series data from experiments to identify chaotic or periodic nature has been an ongoing challenge. Many methods such as Lyapunov Exponents have been put forth to perform such an analysis. Analysis of the periodicity of signals all depend on knowing the various states a system under examination can exist in. However, this leads to a significant downside as the data acquired from experiments is always in a discreet form without no easy means to discover the states of the system[20]. For example, data from the observation of a star's magnetic field cannot be prepared in any way as its not feasible to manipulate the star in any way (at least not with current human technology). The ideal method for time series analysis would be one which works on any arbitrary series without any form of preparation of data. A recent method developed to perform such an analysis of time series is called the Entropy-Complexity Plane (CH-Plane)[21].

The idea for this method first originated in 1995 by Lopez-Ruiz et al. who suggested using complexity as a measure to analyze the periodic or chaotic nature of time series[22]. However, the problem still lay in how to apply the method to an arbitrary time series. This problem was solved by Bandt and Pompe who came up with a method to define a probability array of various states of a time series based on amplitude permutations of the series under analysis allowing it to be completely arbitrary[20]. This method was the final piece needed which allowed Martin et al. to develop the CH Plane. Together with the idea from Lopez-Ruiz et al., they defined a

complexity measure, an entropy measure based on the probability array built using the Bandt-Pompe method with which they then plotted the entropy along the horizontal axis and the complexity along the vertical axis to build the Entropy-Complexity Plane or CH-Plane[21]. A further addition was then later made to the CH-Plane by adding upper and lower bounds to the complexity value that could be seen for each entropy value giving a maximum and minimum curve bounding a valid region[21]. This finally gave the complete CH-Plane as a tool to analyze the nature of time series. This method has been used extensively to analyze time series data in fields of plasma physics[23, 24], neuroscience[25, 26], cardiology[27], economics[28], quantum mechanics[29], image discrimination[30] and more.

2.1 BANDT-POMPE PROBABILITY

The Bandt-Pompe method, alternately called the permutation entropy method, was introduced by Bandt and Pompe to define a probability density array of the various states of a time series. They did this by defining the states as the various permutations of the amplitude of the time series, hence the name permutation entropy[20]. The method is performed as follows:

For a time series $x = \{x_1, x_2, ..., x_T\}$ of length T, it is subdivided into smaller sub-series of length d defined as[20]:

$$e_t = \{x_t, x_{t+1}, ..., x_{t+d-1}\} \; ; \; t \in [1, T-d+1] \tag{2.1}$$

This sub-series length, d, is known as the embedding dimension[20]. The embedded signals are derived for each consecutive element of the time series from the first data point until the $T - d + 1$ data point, giving $T - d + 1$ sub-series which will help define the various states currently contained in the time series[20]. This will now allow us to find the probability density of the states of a system. But to do that, all

the probability states a system can exist in need to be defined first. This is done by considering all the permutations that the amplitude elements of a sub-series of length d can take as the probability states, π_n[20]. This gives us $d!$ probability states. For example, for a embedding dimensions of $d = 3$, the permutation states are:

$$\pi_1 = 1, 2, 3$$

$$\pi_2 = 1, 3, 2$$

$$\pi_3 = 2, 1, 3$$

$$\pi_4 = 2, 3, 1$$

$$\pi_5 = 3, 1, 2$$

$$\pi_6 = 3, 2, 1$$

With the possible states that can exist now defined, the probability of occurrence of these states in the time series can be calculated. To do this, the embedded sub-series are arranged in either ascending or descending order of their amplitudes keeping note of how the positions have been ordered after the sort. This order in which the indices of the amplitudes have been arranged form the states currently existing in the system. These states are then compared to the list of all possible states to see the frequency of occurrence of each possible state. This array of frequency of each state is normalized to the total number of states in the time series, which corresponds to the number of embedded sub-series, to give the probability array or the permutation entropy. Hence, it is defined as[20]:

$$P(\pi) = \frac{\#(t|t \leq T - d + 1, \{x_t, ..., x_{t+d}\} \ has \ type \ \pi)}{T - d + 1} \tag{2.2}$$

Take the following time series as an example:

$$x = 3, 14, 4, 9, 21, 15, 28$$

Using an embedding length of $d = 3$, 5 sub-series will be acquired as follows:

$$e_1 = 3, 14, 4$$

$$e_2 = 14, 4, 9$$

$$e_3 = 4, 9, 21$$

$$e_4 = 9, 21, 15$$

$$e_5 = 21, 15, 28$$

Arranging these sub-series in ascending order of their amplitudes and looking at the position of these elements afterwards;

$$e_1 = 3, 4, 14 \rightarrow 1, 3, 2$$

$$e_2 = 4, 9, 14 \rightarrow 2, 3, 1$$

$$e_3 = 4, 9, 21 \rightarrow 1, 2, 3$$

$$e_4 = 9, 15, 21 \rightarrow 1, 3, 2$$

$$e_5 = 15, 21, 28 \rightarrow 2, 1, 3$$

Now, comparing these to the permutation states, π, of the system, the frequency of repetition of each state, $p(\pi_n)$, can be found.

$$p(\pi_1) = 1$$

$$p(\pi_2) = 2$$

$$p(\pi_3) = 1$$
$$p(\pi_4) = 1$$
$$p(\pi_5) = 0$$
$$p(\pi_6) = 0$$

This array is normalized to the number of sub-series, 5 to get the probability distribution:

$$P(\pi) = 0.2, 0.4, 0.2, 0.2, 0, 0$$

The choice of the embedding dimension is a very important one as it determines the number of states that a time series can access and so, can affect the probability density. Firstly, the embedding dimension, d, must be chosen such that the number of available states, $d!$, is much smaller than the length of the time series[20, 31]. This is to ensure enough sub-series can be extracted to get an accurate representation of the probability density and features do not get obscured. Further, larger embedding dimension can lead to so many accessible states that every feature in the time series amplitude exists as its own individual state resulting in a completely uniform probability density erasing the ability to learn anything about the time series[20, 31]. Another problem with larger embedding dimensions is increased computing time[20, 31]. Hence, Bandt and Pompe suggest using an embedding dimension between 3 and 7[20]. Now, the Bandt-Pompe method has been defined, with which, any arbitrary time series can be analyzed to acquire a probability distribution of states of the system without any sort of preparation of the data or experiment.

2.2 SHANNON ENTROPY

Entropy measure is one of the two quantities used to define the CH-Plane. Entropy quantifies the number of "patterns" that exist in a time series which are represented as the various states in the probability distribution array[21]. The more varied states that exist in the time series, the higher the value of the entropy[21]. For the CH-Plane, Shannon Entropy will be used as the entropy measure.

Shannon entropy is defined based on the probability density of the states of a system. Thanks to the Bandt-Pompe method, a probability density can be defined for any time series which will be used to define the Shannon entropy. For a given probability density, P, the Shannon Entropy is defined as[21]:

$$S[P] = -\sum_{j=1}^{d!} p_j \log(p_j) \tag{2.3}$$

This entropy is normalized to the maximum value of Shannon entropy. This is achieved when every single probability state has equal probability of occurrence, $\frac{1}{d!}$[21].

$$P_{max} = \{p_j = \frac{1}{d!} \; for \; j = 1 \; to \; d!\} \tag{2.4}$$

Using this, the maximum entropy comes out to be $S_{max} = \log(d!)$[21].
So, the normalized Shannon Entropy is[21]:

$$H[P] = \frac{S[P]}{S_{max}} = \frac{S[P]}{\log(d!)} \tag{2.5}$$

Normalized Shannon Entropy takes a value between 0 and 1. Shannon entropy has a low value for periodic series as there are only a few states that are repeated over and

over. Noise on the other hand has a high entropy as it has a lot of different states due to its random nature. Chaotic series have a moderate entropy as they have a large number of states showing up in the time series[21].

2.3 COMPLEXITY

Complexity is the other quantity needed to define the CH-Plane. Complexity is a measure of the level of correlation between the states that exist in a time series[21]. It expresses how closely related the various "patterns" in a time series are. Complexity is defined as[21]:

$$C[P] = H[P]Q[P] \tag{2.6}$$

where $H[P]$ is the Shannon entropy and $Q[P]$ is known as the disequilibrium measure. Many different disequilibrium measures can be used but two of particular focus are the Wooters Distance[21] and the Jensen-Shannon Divergence[21]. A third complexity measure called Fisher Information Measure will also be explored, however, it does not follow the form of equation 2.6[32]. All of these complexity measures will be normalized so that they take a value between 0 and 1.

2.3.1 WOOTERS DISTANCE

The Wooters Statistical Distnce is a measure originally used in Quantum Mechanics to differentiate the various states of a system as well how closely related they are[21]. As such, it is measured with respect to two probability arrays. To measure the complexity of the probability array of an arbitrary time series, it is compared to a uniform probability distribution. For building the CH Plane, the probability array of the time series from the Bandt-Pompe method and the probability array corresponding to the maximum entropy as defined by equation 2.4 are used. Hence, the

normalized Wooters Distance is defined as[21]:

$$Q_W\left[P|P_{max}\right] = \arccos\left\{\sum_{j=1}^{N}(p_j)^{1/2}\left(\frac{1}{N}\right)^{1/2}\right\}\arccos\left\{\left(\frac{1}{N}\right)^{1/2}\right\} \qquad (2.7)$$

Wooters Distance is low for both periodic series and noisy series[21]. Periodic series only have a few states and hence a low level of correlations between states leading to low Wooters Distance. Noisy signals have a lot of states but not a lot of correlation between those states as they are all random leading to low Wooters Distance once again. Chaotic series have a moderate Wooters Distance as they have a significant number of states and hence a significant amount of correlation between those states[21].

2.3.2 JENSEN-SHANNON DIVERGENCE

Jensen-Shannon Divergence is a relative entropy measure and is always measured as a comparison between two probability arrays. They measure the level of correlation between the two probability arrays[21]. Like the Wooters Distance, the probability array from the Bandt-Pompe method will be compared relative to the probability array giving maximum entropy as defined by equation 2.4. Then, the normalized Jensen-Shannon Divergence is defined as[21]:

$$Q_{JS}\left[P|P_{max}\right] = \frac{S\left[\frac{P+P_{max}}{2}\right] - \frac{S[P]}{2} - \frac{S[P_{max}]}{2}}{-\frac{1}{2}\left\{\frac{d!+1}{d!}\log[d!+1] - 2\log[2d!] + \log[d!]\right\}} \qquad (2.8)$$

Where, Q_{max} is defined as[21]:

$$Q_{max} = -\frac{1}{2}\left\{\frac{d!+1}{d!}\log[d!+1] - 2\log[2d!] + \log[d!]\right\} \qquad (2.9)$$

Jensen-Shannon Divergence works the same as Wooters Distance with low values for periodic and noisy series while chaotic series have a moderate value[21].

2.3.3 FISHER INFORMATION MEASURE

The Fisher Information Measure (FIM) is an entropy measure that quantifies the level of disorder in a system[32]. It has been suggested as an alternative measure to Shannon entropy to measure the information entropy of a physical process. The FIM is measured with respect to the probability density array of the system under examination alone unlike the previous two disequilibrium measures. So, the Discreet Normalized Fisher Information Measure is defined as[32]:

$$Q_F[P] = F_0 \sum_{j=1}^{N-1} \left\{ (p_{j+1})^{1/2} - (p_j)^{1/2} \right\}^2 \tag{2.10}$$

Where, F_0 is defined as[32]:

$$F_0 = \begin{cases} 1, \ if \ p_{j^*} = 1 \ for \ j^* = 1 \ or \ j^* = N \ and \ p_j = 0 \ for \ all \ other \ j \\ 1/2, \ otherwise \end{cases} \tag{2.11}$$

FIM works the opposite of Shannon Entropy. Periodic series have a high FIM value while noisy series have a low value[32]. Chaotic series have a moderate value as in all the previous measures[32].

2.4 COMPLEXITY CURVES

There is one final component left to create the CH-Plane. The complexity measures cannot take any value. Since each value of Shannon Entropy corresponds to how many states exist in the time series, there can only exist so many correlations between those existing states. This constrains the complexity between a maximum and minimum value. Over the entire domain of the Shannon Entropy, this constraint

leads to the presence of a maximum and minimum complexity curve. These curves are determined based on geometry and set theory of the probability space[21, 23].

2.5 CH-Plane

With all the components assembled, the CH-Plane can finally be constructed. The Shannon Entropy is plotted along the horizontal axis and the Complexity is plotted along the vertical axis to form the Entropy-Complexity Plane[21]. The maximum and minimum curves are added to the plane completing the CH-Plane[21]. The three CH-Planes that will be studied are the Wooter-Shannon ($C_W \times H$) Plane, Jensen-Shannon ($C_{JS} \times H$) Plane and the Fisher-Shannon ($C_F \times H$) Plane.
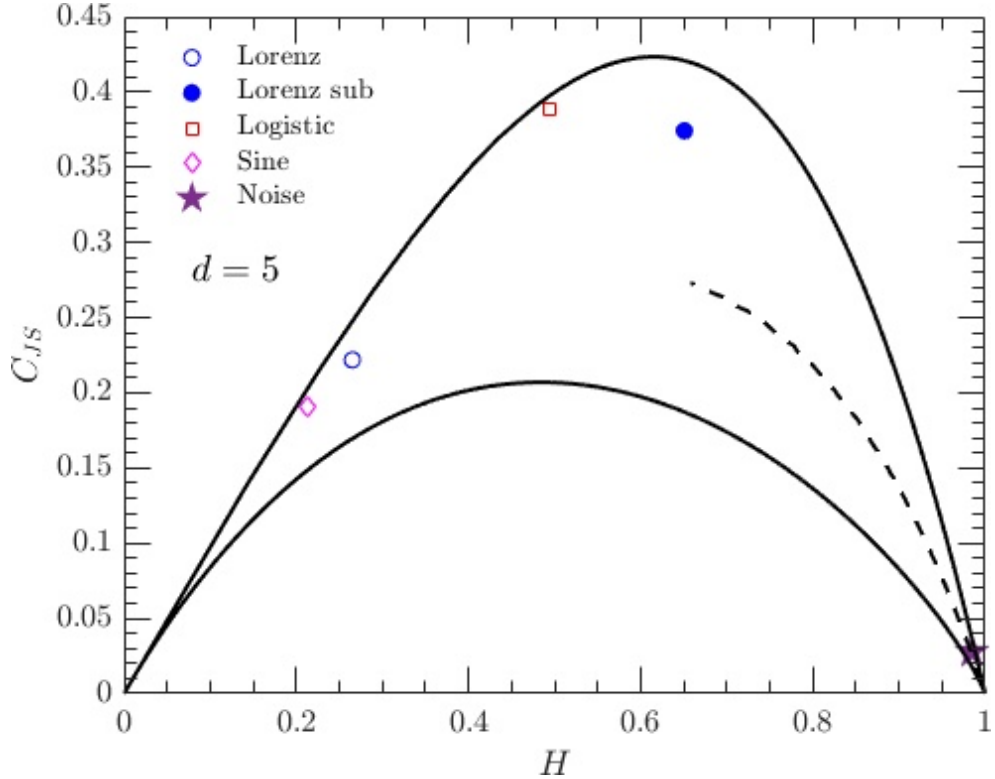
Figure 2.1: Jensen-Shannon Plane is shown with a few signals of varying nature. The dotted line represents Fractional Brownian Motion (fBm) indicating the stochastic region.
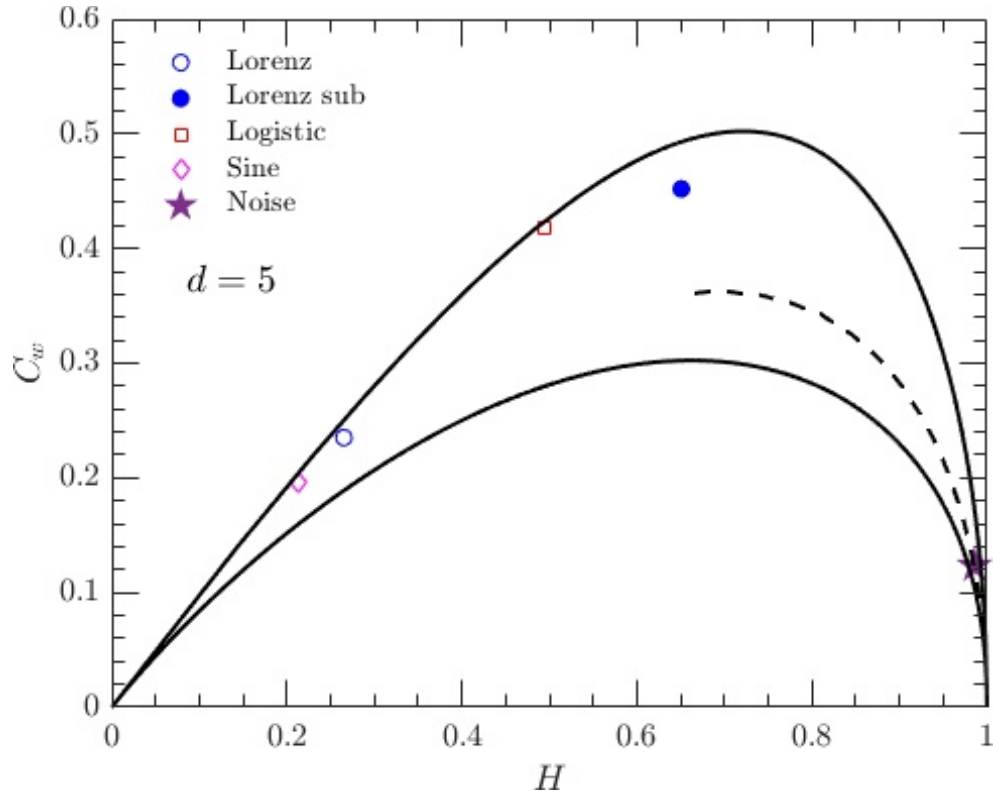
Figure 2.2: Wooters-Shannon Plane is shown with a few signals of varying nature. The dotted line represents Fractional Brownian Motion indicating the stochastic region.

The $C_W \times H$ Plane and $C_{JS} \times H$ Plane behave the same way. Periodic signals are close to the bottom left as they have low entropy and complexity. Noisy signals are at the bottom right as they have high entropy but low complexity. Chaotic signals lie near the middle of the plane close to the maximum complexity curve as they have moderate entropy and complexity. Stochastic signals lie towards the right of the plane midway between the maximum and minimum complexity curve as traced out by the Fractional Brownian Motion (fBm) line. The fractional Brownian motion is a family of Gaussian stochastic processes controlled by the Hurst exponent that are self-similar and show long range dependence[33]. Fractional Brownian motion is one of the simplest stocastic processes to model and hence works as a good measure of

the stochastic region on the CH-Plane. The $C_W \times H$ Plane and $C_{JS} \times H$ are good at differentiating periodic series, chaotic series and noise as they assign them to very clearly differentiated regions in their respective planes[32]. They are however very sensitive to noise.
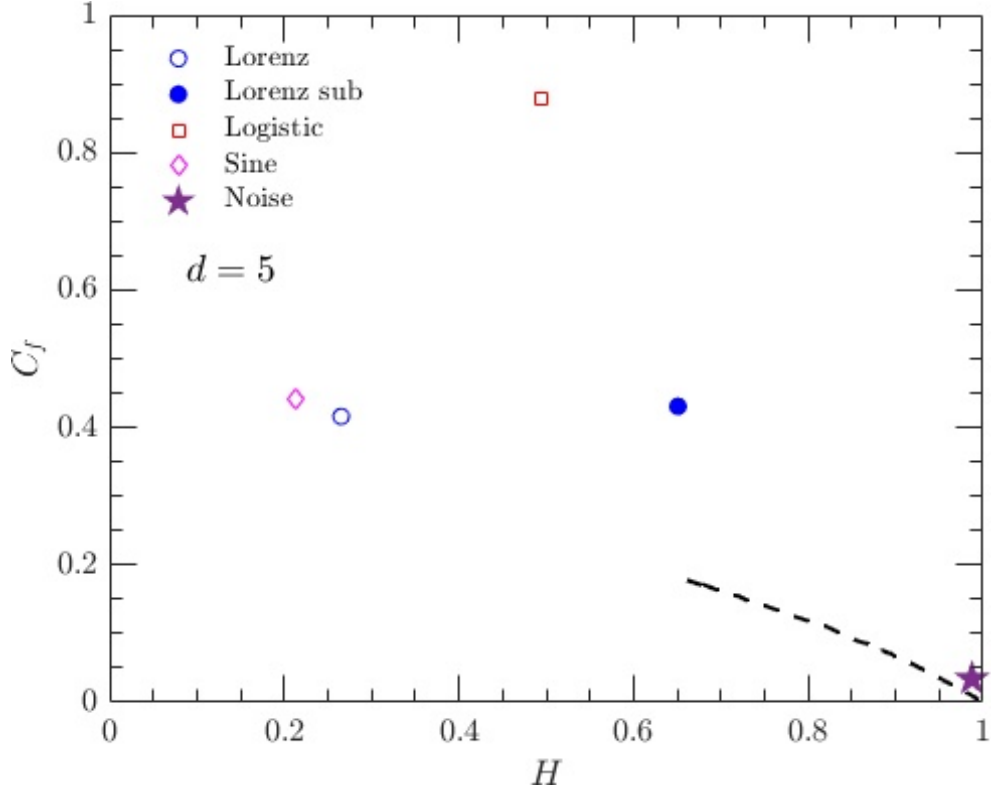
Figure 2.3: Fisher-Shannon Plane is shown with a few signals of varying nature. The dotted line represents Fractional Brownian Motion indicating the stochastic region.

The $C_F \times H$ plane behaves almost opposite to the previous two planes. There are no complexity constraints in this plane as both measures quantify entropy. Periodic signals lie near the top left as they have high FIM but low Shannon Entropy. Chaotic signals lie near the center of the plane as they have a moderate FIM and Shannon Entropy. Noisy signals lie at the bottom right as they have low FIM and high Shannon Entropy. Stochastic signals lie towards the right of the plane closer to the bottom

but still above the noisy signals as shown by the fBm line. The $C_F \times H$ plane is very good at differentiating between different degrees of chaotic nature[32].

Each CH Plane has its own advantages and disadvantages and the CH Plane to be used must be chosen based on the analysis needed to be performed. This thesis will use the Jensen-Shannon CH Plane for analysis.

2.5.1 PERIODIC SIGNALS

Periodic signals, as stated before, are found to lie towards the bottom left of the CH Plane as seen in fig.2.1. However, this is not the full picture. Periodic signals have been found to appear all over the CH Plane depending on two main factors. The first is the ratio between the frequency of the signal (f) and the sampling frequency (f_s)[34]. Periodic signals can lie anywhere along the left edge of the CH Plane close to the maximum complexity curve depending on the frequency ratio as seen in fig.2.4. Signals with lower frequency ratio are closer towards the bottom left and signals with higher frequency ratio are closer to the top left of the plane. The second factor is noise. The presence of noise can move the periodic signal into the chaotic and even noisy regions depending on the signal-to-noise ratio as seen in fig.2.5. Both these factors combined can result in a periodic signal lying in all regions of the CH Plane and can lead to some confusing situations such as a periodic signal falling in the chaotic region. So, extra care must be taken to account for the above factors when applying the CH Plane to periodic signals.

2.5.2 CHAOTIC SIGNALS

Chaotic signals lie in the central region of the CH Plane closer to the maximum complexity curve. They generally have an entropy value between 0.3 and 0.65[21]. Like with the periodic signals, noise can also affect chaotic signals and make them move outside the chaotic regions on the CH Plane. The method used to deal with
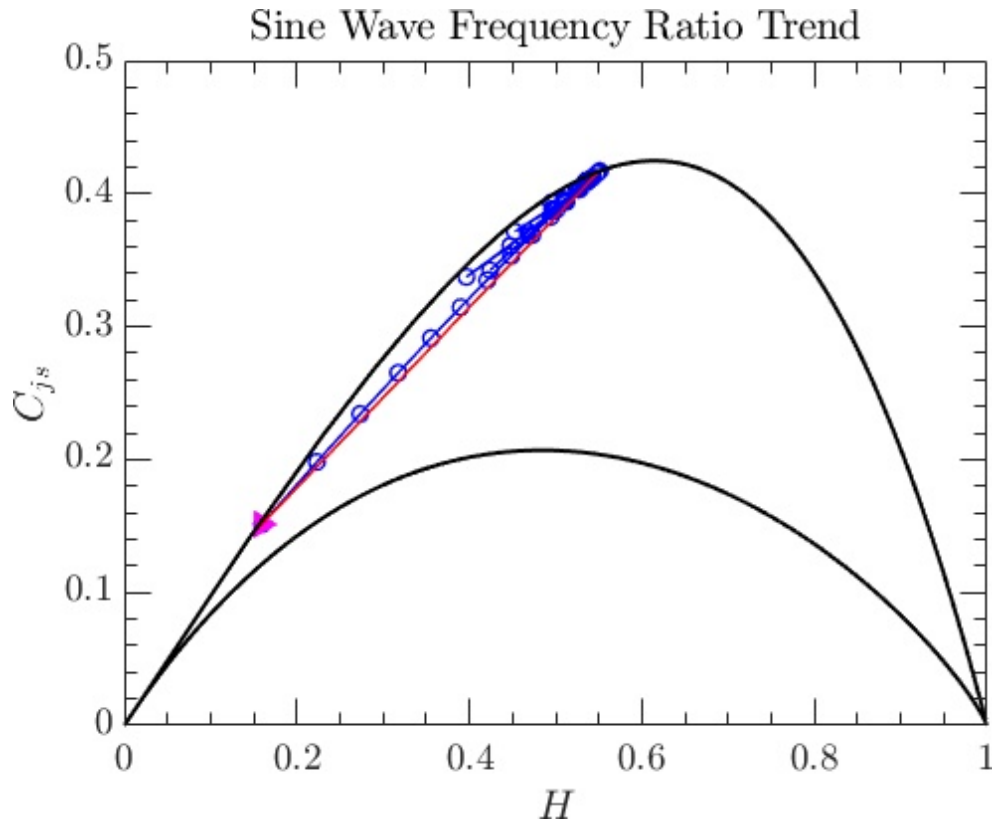
Figure 2.4: The CH Plane location for a sine wave is plotted for various frequency ratios. The triangle at the bottom left represents a 1 Hz sine wave.

noise for chaotic signals is through sub-sampling as seen in 2.6.

2.5.3   SUB-SAMPLING

Sub-sampling of signals is a pre-processing method applied to the time series to reduce the effect of noise when using the CH-Plane. The sub-sampling method focuses on the frequencies of interest in a given time series by changing the sampling frequency and hence the nyquist frequency cutting out any unnecessary high frequency signals which is generally dominated by noise[21, 35].

To perform sub-sampling, the original time series is modified by skipping a regular number of points called the sub-sampling dimension, s[21]. To avoid aliasing, a low-pass filter is applied first to remove the power from the frequencies outside the range of
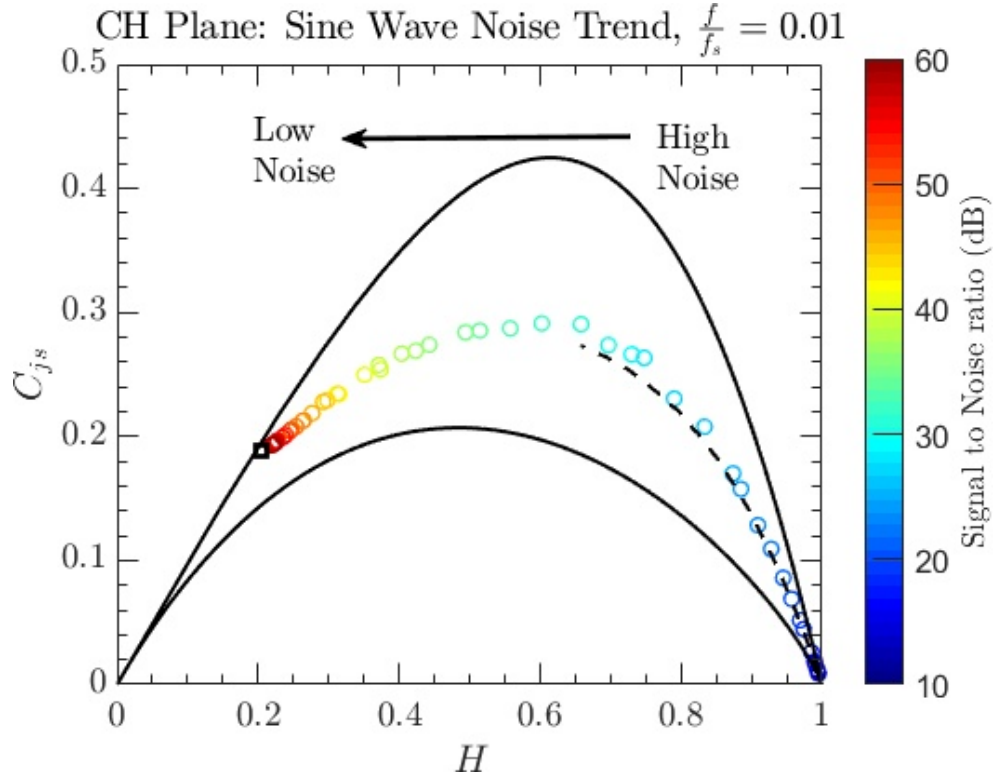
Figure 2.5: The CH Plane location for a sine wave is plotted for various noise levels. The black square represents a sine wave without any noise.

interest. This reduces the sampling frequency to $\frac{f_s}{s}$. So, the sub-sampling dimension must be chosen such that the new sampling frequency only covers the frequencies under study and any other unneeded higher frequencies are eliminated. However, this method has one problem in that the sub-sampled time series has a lower length than the original signal which might not be feasible if the original series was already short. Moreover, aliasing also becomes a problem as power from the cut parts of the series get redistributed into the remaining parts requiring a low-pass filter to be applied first.

To solve these problems, an alternate method called length preserve sub-sampling can be used[35]. As the name suggests, this method sub-samples the series while preserving its original length. In this method, rather than skipping points in the
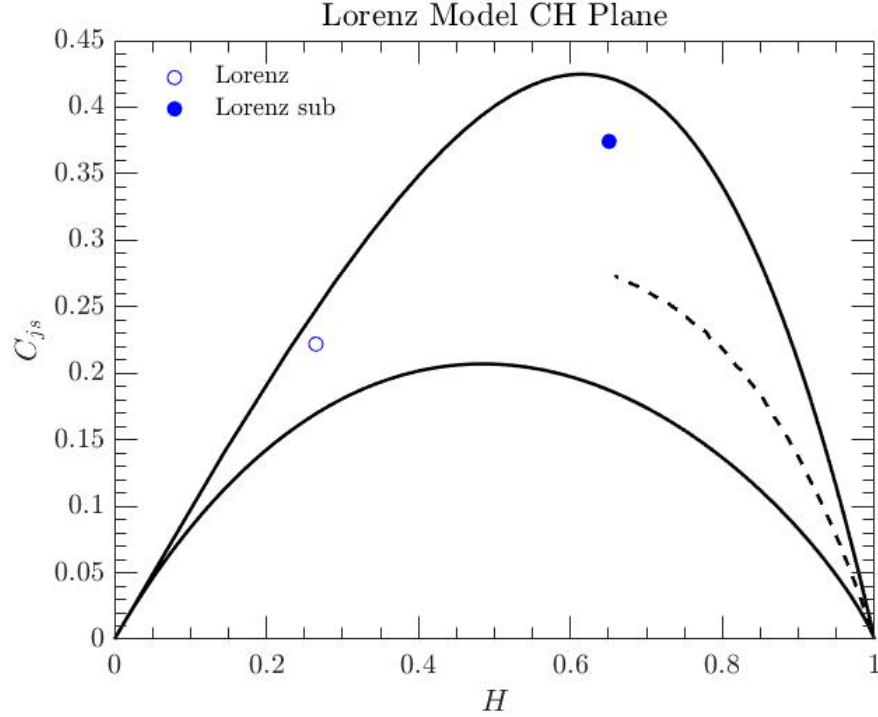
Figure 2.6: The CH Plane location of Lorenz series and its sub-sampled version is shown.

original time series, the points are skipped in the embedded series. For a sub-sampling dimension s, when making the embedded series, instead of taking consecutive points, points are taken every s points away to give a set of embedded series defined as[35]:

$$e_t = \{x_t, x_{t+s}, ..., x_{t+(s \times (d-1))}\} \; ; \; t \in [1, T - (s \times (d-1))] \tag{2.12}$$

The embedded signals are started from every consecutive point as before. This way, every single point in the original time series is accounted for while the sampling frequency is still reduced to the region of interest as before. This way, both the problem of length reduction and power aliasing is solved. The rest of the CH Plane methodology is performed as usual.

2.5.4 STOCHASTIC SIGNALS AND NOISY SIGNALS

Stochastic signals tend to lie towards the right of the CH Plane with entropy value greater than 0.4 and a moderate complexity value in the middle between the maximum and minimum complexity curves as indicated by the Fractional Brownian Motion line in fig.2.1[21].

White noise signals all lie towards the bottom right of the CH Plane[21]. White noise is a type of stochatic signal with zero mean, finite variance and the covariance matrix of

$$Cov(x_i, x_j) = 0 \; for \; all \; i \neq j \qquad (2.13)$$

The CH Plane is very sensitive to noise[21, 32]. So, adding noise to the other three types of signals can result in them falling towards the bottom right of the plane. This is the reason noise analysis and sub-sampling are used before applying the CH Plane.

2.6 SUMMARY

The CH-Plane is a tool used to analyze the nature of signals; whether they are periodic, chaotic, stochastic or noisy. The CH-Plane was built by Martin, Rosso et al as a tool to analyze the nature of any arbitrary time series without any pre-preparation of data needing to be built into the experiment.

The CH-Plane method first uses the Band-Pompe permutation entropy method to acquire a probability density array of various amplitude permutations in a time series. Using this probability density array, the entropy and complexity are calculated. For entropy, Shannon entropy is used while for complexity, Jensen-Shannon Divergence is used. Plotting the entropy along the horizontal axis and complexity along the vertical axis along with two extrema curves that define the upper and lower limits to

complexity at every entropy value gives the full CH-Plane.

On the CH-Plane, periodic signals are considered to occupy the bottom left region, however, they can in fact be found all over the plane depending on ratio of frequency of the signal to sampling frequency and noise level. For the remaining natures, chaotic signals fall near the middle of the plane close to the maximum complexity curve, stochastic signals fall towards the right midway between the complexity curves, and noisy signals fall to the bottom right. A method of pre-processing called sub-sampling can be used to focus the time series onto frequencies of interest.

All of this together, gives the CH-Plane tool that will be used to analyze the data from plasma experiments for this project.

CHAPTER 3.

TIME SERIES ANALYSIS OF FLUCTUATIONS IN A PLASMA EXPERIMENT

Filamentary structures are common in many plasmas seen in the universe from space plasmas to plasma devices on Earth[2, 36]. These filamentary structures can drive temperature and density fluctuations in the plasma which can determine the transport mechanisms. These filamentary structures are closely connected to the plasma edge region of confinement devices where they can drive non-linear drift wave-type fluctuations[36]. This results in a need to understand the fluctuations due to filamentary structures to better build and control plasmas in experimental settings better. This motivates an analysis of plasma experiments around temperature filaments to see if these fluctuations and transport are chaotic or stochastic in nature.

3.1   EXPERIMENTAL SET-UP

The experiment was performed using the Large Plasma Device (LAPD) at the Basic Plasma Facility, UCLA[36, 37]. The LAPD is made of a cylindrical chamber 18 m in length and 60 cm in diameter surrounded by solenoidal field coils to produce a uniform magnetic field[36, 37]. There is a Barium Oxide cathode at one end of the chamber and a mesh anode 50 cm away from the cathode. The chamber is
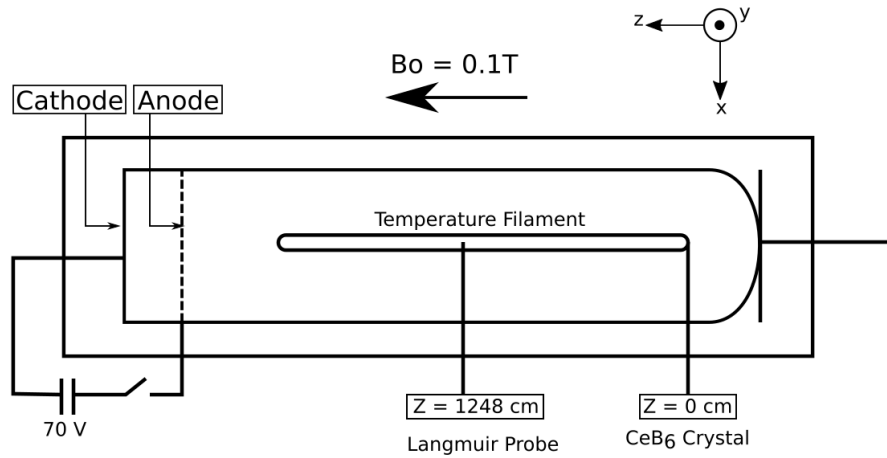
Figure 3.1: The schematic of the Large Plasma Device is shown. The plasma chamber is 18 m in length and 60 cm in diameter. A constant magnetic field of 0.1T is applied along the length of the chamber pointing towards the cathode. The cathode crystal is inserted at port 0 while the langmuir probe is inserted at port 39.

filled with helium gas at a pressure of 1.28×10^{-5} torr[36, 37]. The Helium plasma is created through collisional ionization with electrons. The LAPD also has ports spaced 32 cm apart along its length which are used to insert probes and devices into the plasma[36, 37]. These ports are used to insert the crystal cathode used as a heat source and the Langmuir probe used to measure the plasma parameters.

To create the temperature filament in the plasma, a 3 mm diameter Cerium hexaboride crystal cathode is used[36]. The crystal is ohmically heated to generate an electron beam. The electrons conduct down along the length of the plasma column in the direction of the magnetic field to create a long and thin filament of higher temperature region in the plasma which extends to less than 10 m in length and 20 mm in diameter[36]. This temperature filament acts as the source of fluctuations in the experiment. The cathode is mounted onto a probe and inserted into the plasma column through the ports on the side of the LAPD at port 39[36].

3.1.1 LANGMUIR PROBE

Langmuir probes are devices used to measure plasma parameters such as temperature, density and potential in cold plasmas[38]. This is done by measuring the electron or ion current which is related to the plasma parameters. Langmuir probes usually consist of a metallic wire or surface that is inserted into the plasma and biased with respect to a reference electrode to draw an electron or ion current as needed based on the measurements required[38].

The Langmuir probe is generally used to measure ion saturation current. When the Langmuir probe is biased at a voltage lower than the plasma potential so that it is negatively charged with respect to the background, it draws in the positive ions[38]. This flow of ions is called the ion saturation current and it continues till the probe potential reaches the plasma potential at which point, the ions start getting repelled. The ion saturation current, when electron temperature is greater than ion temperature, is related to the plasma parameters as follows[38]:

$$I_{sat} \approx enA_{probe}\sqrt{\frac{kT_e}{m}} \tag{3.1}$$

Here, A_{probe} is the area of the collecting surface of the probe, T_e is the electron temperature and n is the plasma density. The ion saturation current measured by the Langmuir probe is independent of the shape of the collecting surface and only depends on its area. From the saturation current, the required plasma parameters can be extracted. As the experiment is analyzing fluctuations, the temperature fluctuations to the first order, δT_e, are extracted from saturation current fluctuations, δI_{sat}, as[39]:

$$\delta T_e \approx 2\langle T_e \rangle \left(1 - \sqrt{1 - 2\frac{\delta I_{sat}}{\langle I_{sat} \rangle}}\right) \tag{3.2}$$

The floating potential can also be measured from the Langmuir probe as follows[38]:

$$V_f = V_p + \left(\frac{kT_e}{e} \right) \log \left(\sqrt{\frac{2\pi m_e}{m_i}} \right) \tag{3.3}$$

In the above experiment, a Langmuir probe is inserted through the ports on the side of the LAPD to measure the saturation current. The probe is mounted on drivers that can be programmed to sweep the plasma spatially with a movement accuracy of less than 1 mm.

3.2   Experimental Procedure

The experiment is conducted in the afterglow phase of the plasma. The main BaO cathode is biased by -70 V with respect to the anode to create a beam of thermionic electrons into the cylindrical chamber which then creates the He plasma through collisional ionization with the He gas in the chamber[36]. The plasma column created is magnetically confined by the 0.1 T magnetic field and fills the whole chamber. This is the main discharge phase of the plasma and it has an electron temperature of 5 eV and a density of 2×10^{12} cm^{-3} in this phase[36]. After 12 ms, the bias is turned off and the plasma moves into the afterglow phase where the electron temperature drops to less than 0.25 eV[36]. The experiment is conducted during this phase.

The crystal heat source is activated 2 ms into this phase by biasing the crystal cathode -20V with respect to the anode and the bias is maintained for 20 ms[36]. This generates a long filament of higher temperature in a cold plasma background. A Langmuir probe mounted on an automated probe drive is inserted at port 39[36]. To collect data, the probe is placed at one point and saturation current is measured. This is repeated for multiple shots. Then, the probe is moved to another spatial location and the process is repeated[36]. This is done until a $1cm \times 1cm$ plane is traced out.

This process is then repeated to measure the floating voltage by passing the current through a resistor. This method of data taking works due to high reproducibility of the plasma conditions in each run[36].
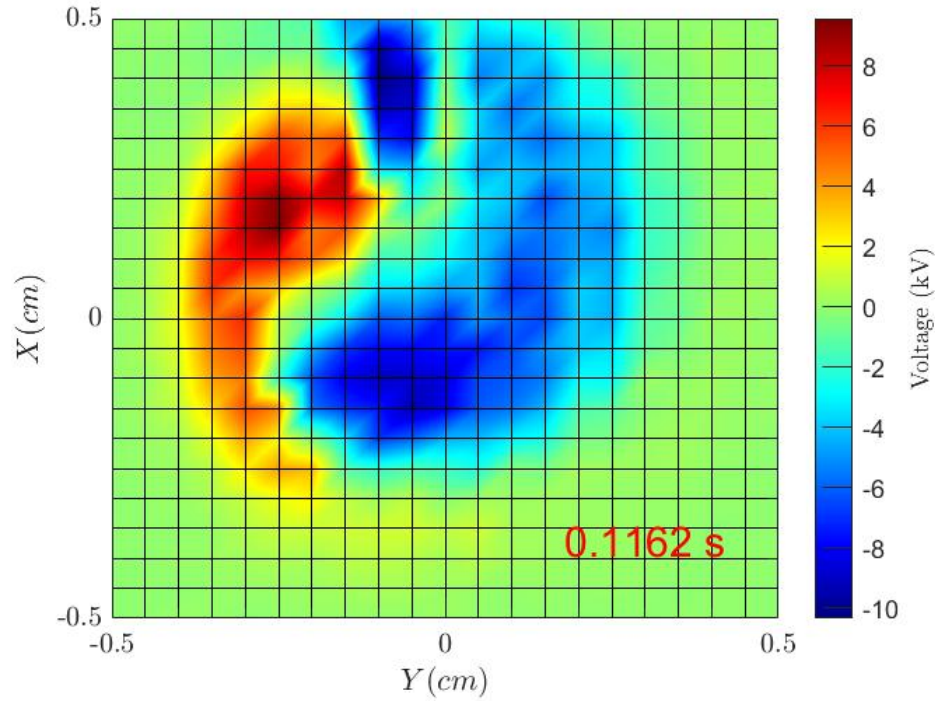
Figure 3.2: The $1cm \times 1cm$ plane of floating voltage measured by the Langmuir probe captured at 0.1162 ms after the cathode is turned on and the temperature filament is generated is shown.

3.3 RESULTS

The saturation current is measured radially from the center of the heat source to a distance of 2.7 cm. The saturation current has two main regions: a periodic region for the first 4 ms and a chaotic region for the remaining 11 ms as seen in fig.3.3.

The floating voltage is measured by the probe in a 1 cm x 1 cm plane containing the heat source as seen in fig.3.2. The voltage time series is measured for 40 ms. It has
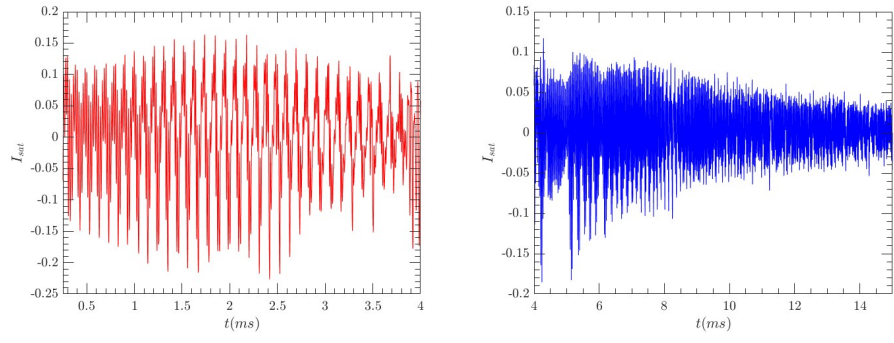
(a) Time Series: Periodic Section   (b) Time Series: Chaotic Section
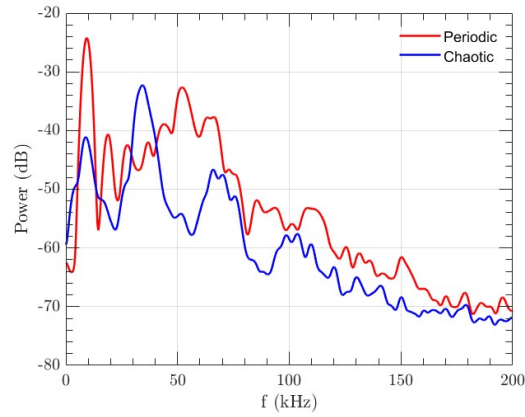
(c) Power Spectrum

Figure 3.3: The results of ion saturation current measured at a distance of 0.3 cm
radially away from center of heat source is shown. The top left panel shows the
saturation current for 0-4 ms while the top right panel shows the saturation current
for 4-15 ms. The bottom panel shows the power spectrum of the saturation current
seen in the top two panels.

two main regions: a periodic region for the first 7 ms and a chaotic region for the

remaining 13 ms as seen in fig.3.4.

(a) Time Series: Periodic Section

(b) Time Series: Chaotic Section

(c) Power Spectrum
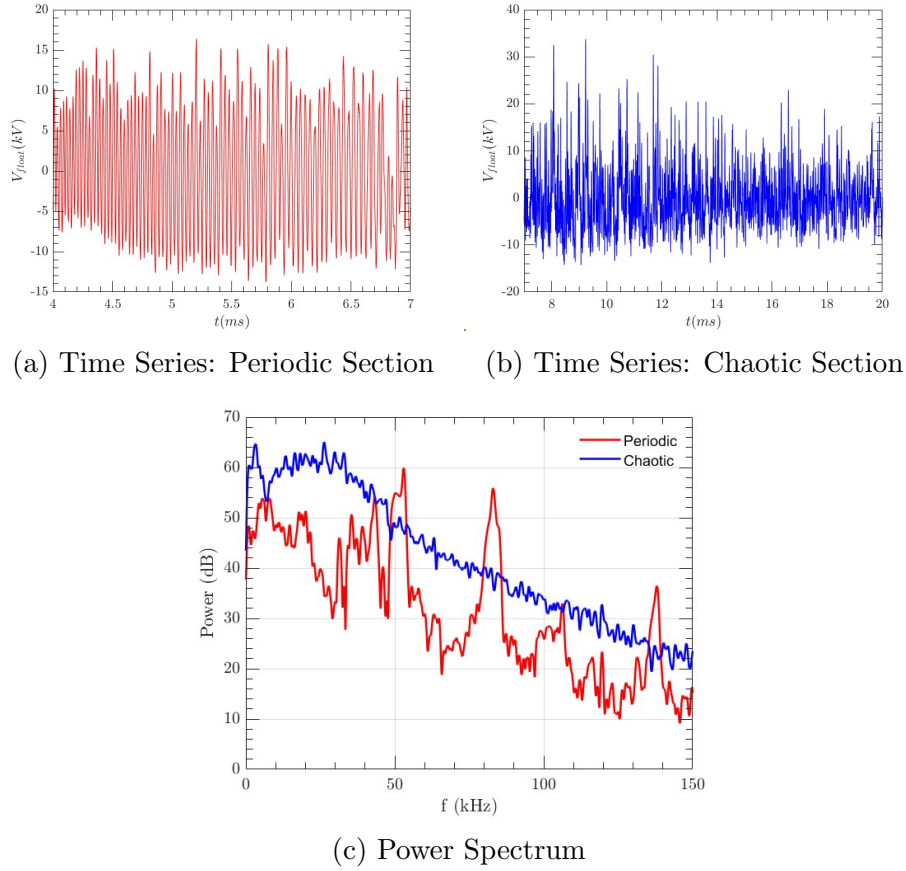
Figure 3.4: The results of the floating voltage measured at a distance of 0.1 cm radially away from center of heat source is shown. The top left panel shows the floating voltage for 4-7 ms while the top right panel shows the floating voltage for 7-20 ms. The bottom panel shows the power spectrum of the floating voltage seen in the top two panels.

3.4 ANALYSIS

3.4.1 SATURATION CURRENT

fig.3.5 shows the CH plane for the first 4 ms of the saturation current. We can see from fig.3.5a that the CH plane matches with the periodic signal CH plane shown in fig.2.5 showing that the first section of the saturation current time series is periodic. The CH Plane for the remaining 10 ms is shown in fig.3.6. The region originally

falls along the fractional brownian motion as seen in fig.3.6a making the region look stochastic. However, once the time series is subsampled to focus on the frequencies of interest; the first 500 kHz exponential region seen in the power spectrum in fig.3.3c, the time series moves into the chaotic region of the CH Plane as seen in fig.3.6b. This shows that the heat transport starts as a periodic process and then transitions to a chaotic process. However, the transition to chaos is not very well seen in the current data. At radii further away from the center, the time series starts to look more stochastic even with subsampling due to the presence of noise. This effect is more pronounced further away from the center as the amplitude of the current series drops and noise dominates more.

(a) Periodic Section

(b) Periodic section subsampled

Figure 3.5: The CH Plane positions of the periodic segment of the saturation current time series at various radii is shown. The left panel shows the result for the original time series while the right panel shows the results for the subsampled time series. The radial profile of the saturation current is shown in the inset plot.

(a) Chaotic section

(b) Chaotic Section subsampled
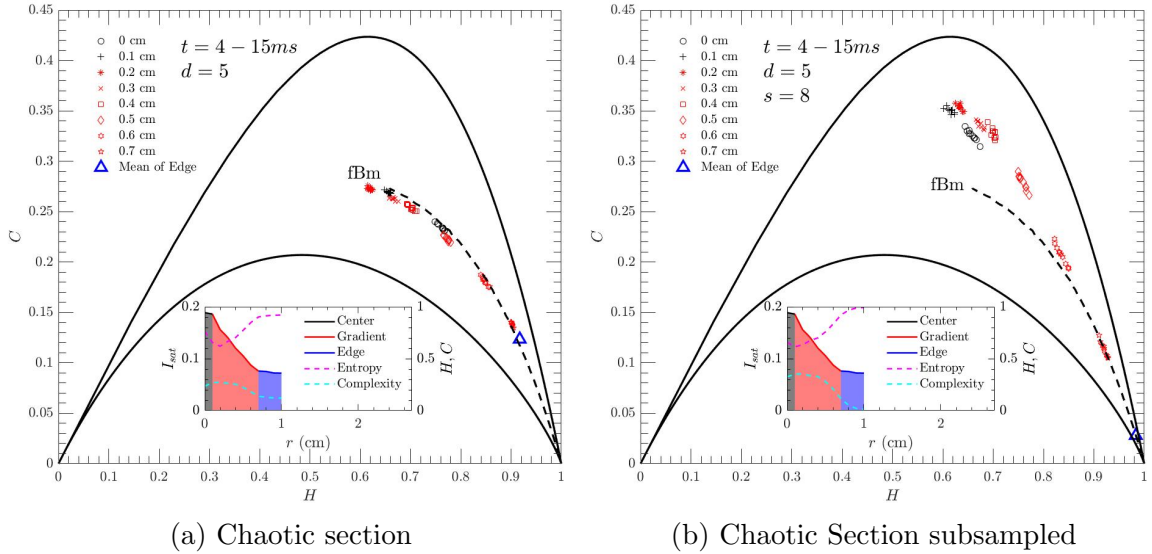
Figure 3.6: The CH Plane positions of the chaotic segment of the Saturation current time series at various radii is shown. The left panel shows the result for the original time series while the right panel shows the results for the subsampled time series. The radial profile of the saturation current is shown in the inset plot.

3.4.2 Floating Voltage

(a) Periodic Section

(b) Periodic section subsampled

Figure 3.7: The CH Plane positions of the periodic segment of the floating voltage time series at various radii is shown. The left panel shows the result for the original time series while the right panel shows the results for the subsampled time series.

(a) Chaotic section

(b) Chaotic Section subsampled

Figure 3.8: The CH Plane positions of the chaotic segment of the floating voltage time series at various radii is shown. The left panel shows the result for the original time series while the right panel shows the results for the subsampled time series.

To see this transition better, the voltage data is also analyzed. The CH Planes in fig.3.7 and fig.3.8 show the CH Plane for the floating voltage data. fig.3.7a shows the CH plane location for the first 7 ms of the data. fig.3.7b shows the location of the same data when subsampled down. As in the case with the current data, the voltage data follows the periodic trend established in fig.2.5 in both the unsubsampled and subsampled cases. This shows that the first 7 ms is clearly periodic. The CH Plane for the next 13 ms is shown in fig.3.8. As in the current time series, the voltage series originally falls in the middle of the plane between the complexity curves along the fBm line making it look stochastic. But, once subsampled to focus on the frequencies of interest; the first 150 kHz showing the exponential trend in the power spectrum in fig.3.4c, the time series moves very clearly up into the chaotic region. All of the radii from the center to all the way out are clearly in the chaotic region and are not spread out into the stochastic region unlike the current data. So, the voltage data clearly shows the latter 13 ms is chaotic in nature better than the current data. This also indicates that the voltage data suffers less disruptions from noise. This also shows

very definitively that the exponential trend in power spectrum is a good indicator for
chaotic nature as subsampling both the current and voltage time series to focus on
this region makes the data move into the chaotic region of the CH Plane.

This indicates overall that the cross field heat transport starts off classical and
then slowly changes to be anomalous in the presence of a filamentary heat source.
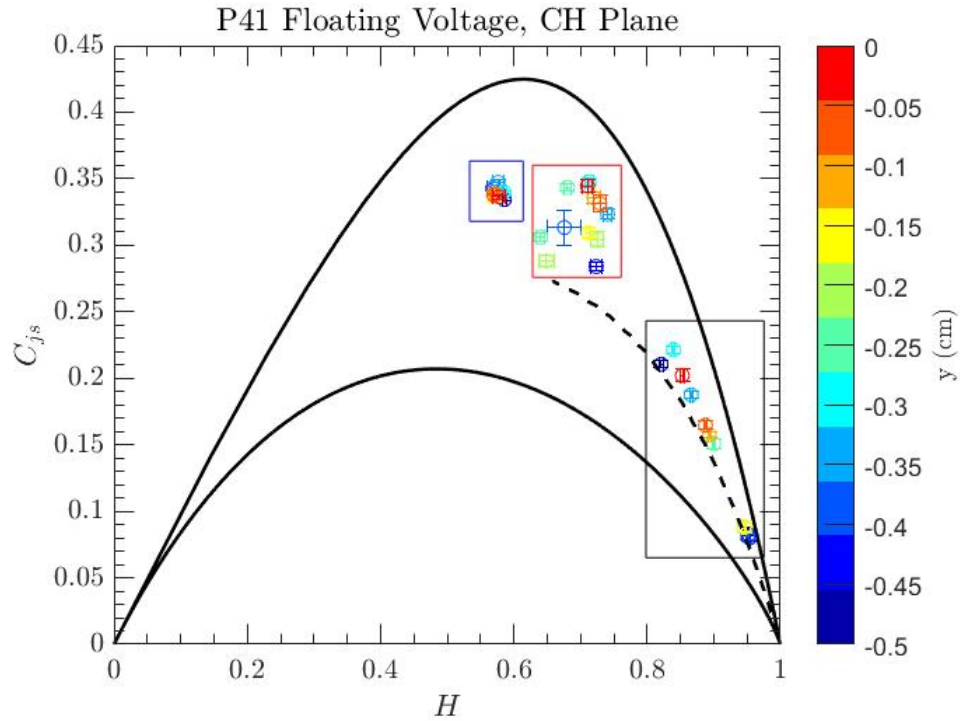
Figure 3.9: The CH Plane of the subsampled floating voltage time series data for
periodic region (red box), chaotic region (blue box) and background plasma (black
box) from the center of heat source up to 0.5 cm away.

3.5 SUMMARY

The CH Plane is used to analyze current and voltage data acquired from a plasma
experiment about cross field heat transport from filamentary temperature region in
a cold plasma. From analyzing both the current and voltage data, it is seen that
when the heat source is turned on, the transport starts out periodic for the first 4-7

ms before transitioning to be chaotic for the remaining period that the heat source is maintained. It is also found that voltage is more robust to disruptions from noise as opposed to current. Moreover, the chaotic nature is found to be clearly seen when the time series is subsampled to focus on the exponential region of frequencies seen in the power spectrum showing that this exponential region is an indication of chaotic dynamics.

CHAPTER 4.

NON-LINEAR TIME SERIES ANALYSIS: HURST EXPONENT

The Hurst exponent is a measure introduced by Edwin Hurst as a way to quantify the long term memory and persistence of a time series in 1951 during his research about dam construction on the river Nile[40, 41]. Hurst exponent takes a value between 0 and 1. A Hurst exponent less than 0.5 indicates anti-persistent nature meaning that if the time series was previously increasing, the time series in the future will be decreasing and vice versa[42]. Conversely, a Hurst exponent greater than 0.5 indicates persistent nature meaning that if the time series was previously increasing, the time series in the future will continue to be increasing[42]. Hurst exponents have been used to analyze plasma turbulence[43], atmospheric phenomena[44], fluid flows[45], aeronautics[46] and more.

There have been multiple methods introduced to calculate the Hurst exponent such as Rescaled Range method[40, 47, 48], Detrend Fluctuation Analysis[40, 47, 49] and wavelet methods[47]. The analysis provided below uses the Rescaled Range method to calculate the Hurst exponents.

4.1 RESCALED RANGE METHOD

The Rescaled Range (R/S) method is one of the main methods used to find the Hurst exponent of a time series. The rescaled range is calculated by dividing the

range by the standard deviation and is performed as follows.

For a given time series $X = \{x_i, i = 1, 2, ..., N\}$ of length N, it is broken into smaller sub-samples of length n from $n = \{2, 3, ..., N\}$[50]. The rescaled range is calculated for each sub-sample by dividing the range by the standard deviation. The standard deviation of the sub-sample is calculated as[50]:

$$S(n) = \sqrt{\frac{1}{n} \sum_{i=1}^{n} x_i - \bar{X}} \qquad (4.1)$$

Then, to calculate the range, first the mean of the subsample is calculated[50]:

$$\bar{X} = \frac{1}{n} \sum_{i=1}^{n} x_i \qquad (4.2)$$

Then, the mean adjusted series is calculated by subtracting the mean from each element of the sub-sample as[50]:

$$B_k = x_k - \bar{X}, \ k = 1, 2, ..., n \qquad (4.3)$$

Then a cumulative sum series is calculated from the mean adjusted series as[50]:

$$D_k = \sum_{j=1}^{k} B_j, \ k = 1, 2, ..., n \qquad (4.4)$$

Now, the range is calculated as the difference between the maximum and the minimum value of the cumulative sum series, D[50]:

$$R(n) = max\,(D_1, D_2, ..., D_n) - min\,(D_1, D_2, ..., D_n) \qquad (4.5)$$

The range is then rescaled by the standard deviation by just dividing them[50]:

$$Q(n) = \frac{R(n)}{S(n)} \tag{4.6}$$

The above rescaled range series can be used to find the Hurst exponent of the time series as[50]:

$$Q(n) = Cn^H \tag{4.7}$$

By plotting the rescaled range, Q and the subsample length, n, on a log-log plot and fitting it to a straight line, the Hurst exponent can be found from the slope[50].

4.2 SYNTHETIC EXAMPLES

To see the rescaled range method in action, it is performed on the sine wave and two common types of chaotic maps: the Lorenz series and the Logistic map.

(a) Time Series   (b) Rescaled Range Plot
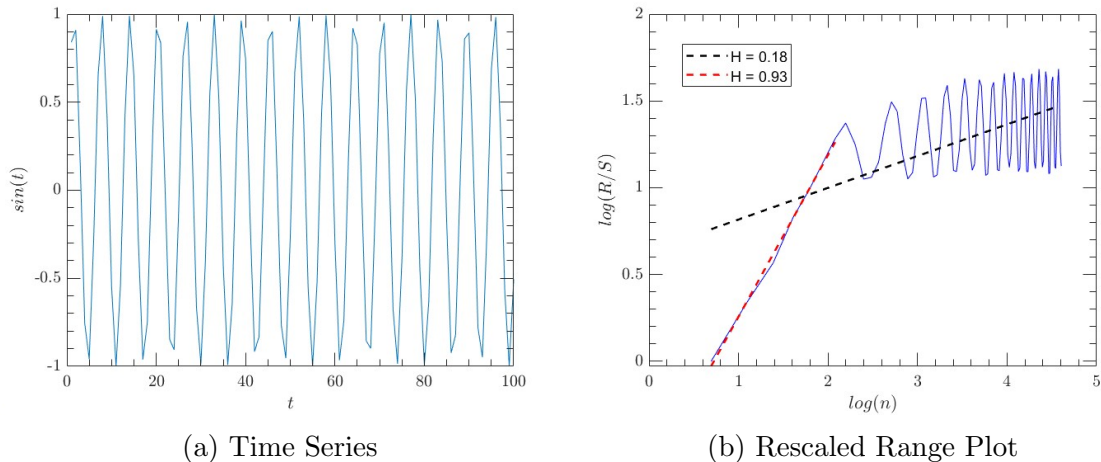
Figure 4.1: The results of the rescaled range analysis of a Sine Wave is shown. The left panel shows the sine wave used for analysis. The right panel shows the rescaled range plotted against the scale length on a log-log scale. A linear trend and an oscillatory trend are seen in the rescaled range and are fit by separate linear fits indicated by the dotted lines.

Periodic signals like sine waves show two regimes of Hurst exponent as seen in
fig.4.1b. The first regime of rescaled range gives a Hurst exponent close to 1 showing
strong persistence behaviour[50]. The second regime of the rescaled range shows an
oscillatory pattern and can be used to extract out the period of the signal[50]. This
pattern for the rescaled range is a good indicator of periodic behaviour in a time
series.

(a) Time Series

(b) Rescaled Range Plot
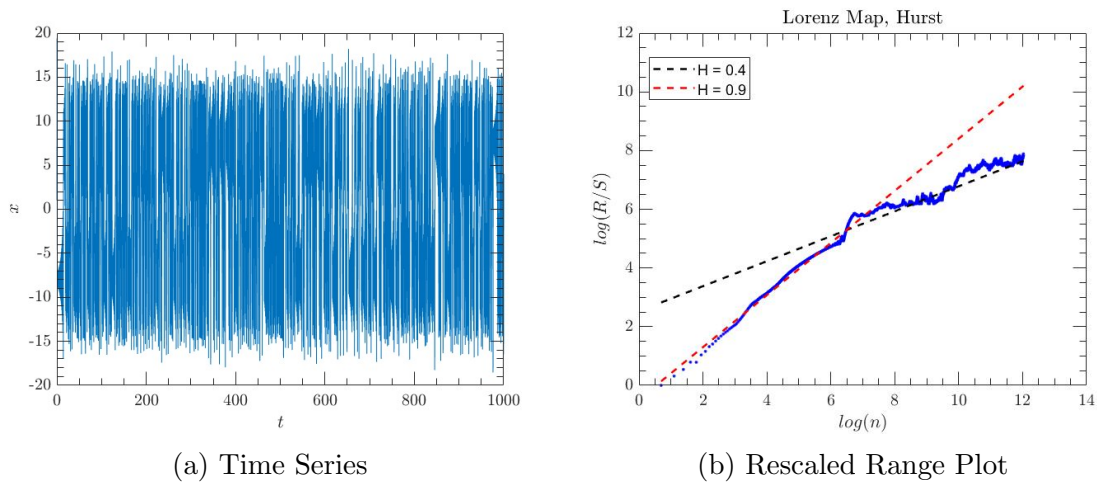
Figure 4.2: The results of the rescaled range analysis of the Lorenz system for $\beta = 7/3$,
$\rho = 28$ and $\sigma = 10$ is shown. The left panel shows the time series solution in $\hat{x}$
direction. The right panel shows the rescaled range plotted against the scale length
on a log-log scale. Two different linear trends are seen in the rescaled range and are
fit by separate linear fits indicated by the dotted lines.

The Lorenz system is the most well known model of a chaotic system and is used
to model the chaotic nature of weather phenomenon[51]. It was introduced by Lorenz
in 1963 to model the convection of particles in a two dimensional fluid cell that was
heated from below and cooled from above[51–53]. The Lorenz model is acquired from
the fourier transform in two dimensions of the Navier-Stokes equations governing the
fluid convection in the fluid cell truncated to only three modes[51, 53]. The Lorenz
model is a system of three differential equations parameterized by three variables β,

ρ and σ as follows[51–53]:

$$\frac{dx}{dt} = \sigma(y - x) \tag{4.8}$$

$$\frac{dy}{dt} = x(\rho - z) - y \tag{4.9}$$

$$\frac{dz}{dt} = xy - \beta z \tag{4.10}$$

Here, x gives the convective fluid motion, y gives the horizontal temperature variation and z gives the vertical temperature variation all under the influence of gravity[51–53]. Further, σ is the Prandtl number, ρ is the Rayleigh number and β is a geometric factor[51–53]. Solving the above system of differential equations gives three time series; x(t), y(t) and z(t). The solutions can be a chaotic time series depending on the values of β, ρ and σ[51–53]. This series has a double scroll pattern with two stable equilibrium points that the series tends towards[51–53]. A particle in the Lorenz system has motion on two time scales: a short time scale motion where a particle orbits around one of two fixed points and a long time scale where the particle orbits around the whole system[50–52]. The Lorenz series shows two Hurst exponent values as seen in fig.4.2. The rescaled range plot shows that the first section has a higher Hurst exponent at $H = 0.8$ while the latter section has a lower Hurst exponent at $H = 0.4$. These two Hurst exponents correspond to the two time scales of motion present in a Lorenz system. The first segment corresponds to the short time scale behaviour while the second segment corresponds to the long time scale motion[44, 50]. Moreover, one Hurst exponent is above 0.5 while the other is below 0.5 showing the presence of both persistence and anti-persistence in the Lorenz map. The short time scale Hurst exponent is greater than 0.5 indicating persistence showing the tendency to maintain the orbit around the fixed point. Meanwhile, the long time scale Hurst exponent is less than 0.5 indicating anti-persistence showing the tendency

to eventually decay into the orbit around one of the fixed point.

(a) Time Series

(b) r = 3
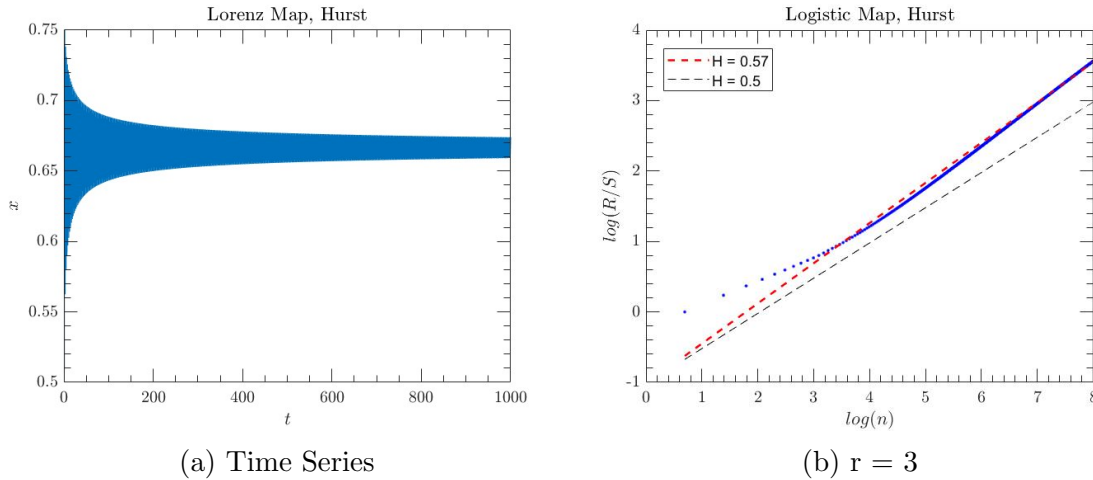
Figure 4.3: The results of the rescaled range analysis of the logistic map for r = 3 is shown. The left panel shows the time series. The right panel shows the rescaled range plotted against the scale length on a log-log scale. The H=0.5 Hurst exponent fit line is indicated by the black dotted line.

(a) Time Series

(b) r = 3.7
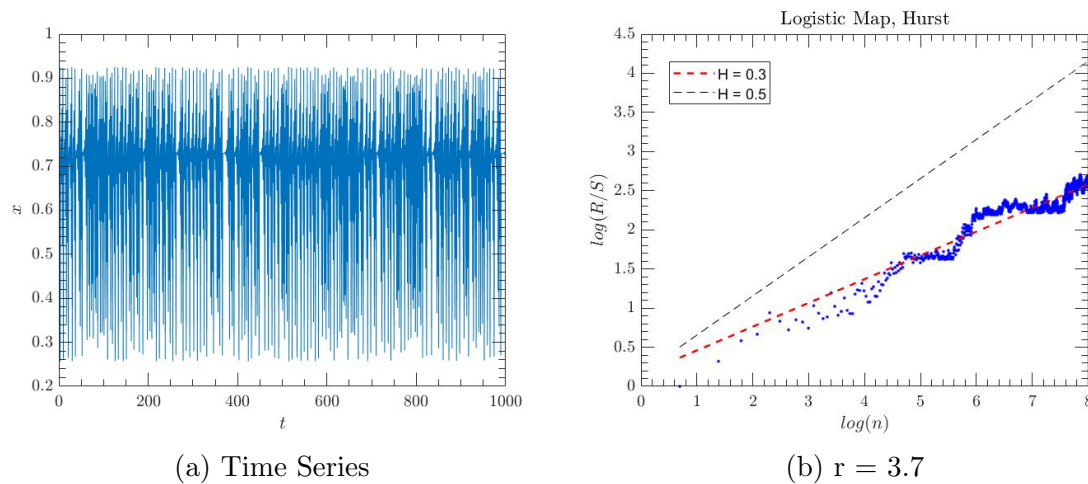
Figure 4.4: The results of the rescaled range analysis of the logistic map for r = 3.7 is shown. The left panel shows the time series. The right panel shows the rescaled range plotted against the scale length on a log-log scale. The H=0.5 Hurst exponent fit line is indicated by the black dotted line.

The logistic map is another common chaotic map. It is a discreet time series based

on the logistic equation[54]:

$$x_{n+1} = rx_n(1 - x_n) \tag{4.11}$$

The logistic map is used to model population growth and a r-value greater than 3.4 gives a chaotic nature to the time series[54]. It is a chaotic series with only a single time scale. The logistic map shows only a single Hurst exponent as seen in fig.4.3 and 4.4. fig.4.3b shows only a Hurst exponent greater than 0.5 indicating persistence while fig.4.4b shows only a Hurst exponent less than 0.5 indicating anti-persistence. Moreover, they both only show a single Hurst exponent. This shows that the logistic series only has a single time scale behaviour[44, 50].

4.3 EXPERIMENTAL DATA ANALYSIS

Hurst exponent for the periodic section are shown for the current in fig.4.5 and the voltage in fig.4.6. The current rescaled range very clearly shows a linear high Hurst exponent for the first region while the second region shows oscillations like the sine wave Hurst exponent in fig.4.1b. While the second region is not seen in the voltage rescaled range in fig.4.6b, the rescaled range still has a linear trend with a Hurst exponent close to one. This confirms that the first few milliseconds of the electron transport from the filament are periodic in nature before changing to be more chaotic.

The Hurst exponents of the chaotic regions are shown in fig.4.7 for the current data and fig.4.8 for the voltage data. They both show double Hurst exponents in chaotic regions of the time series similar to the chaotic Lorenz series. This double Hurst exponent is very clearly seen in the saturation current time series. As seen in fig.4.7b, the saturation current time series shows Hurst exponents of $H = 0.2$ and $H = 0.9$ indicating the presence of both persistent and anti-persistent features.

(a) Time Series
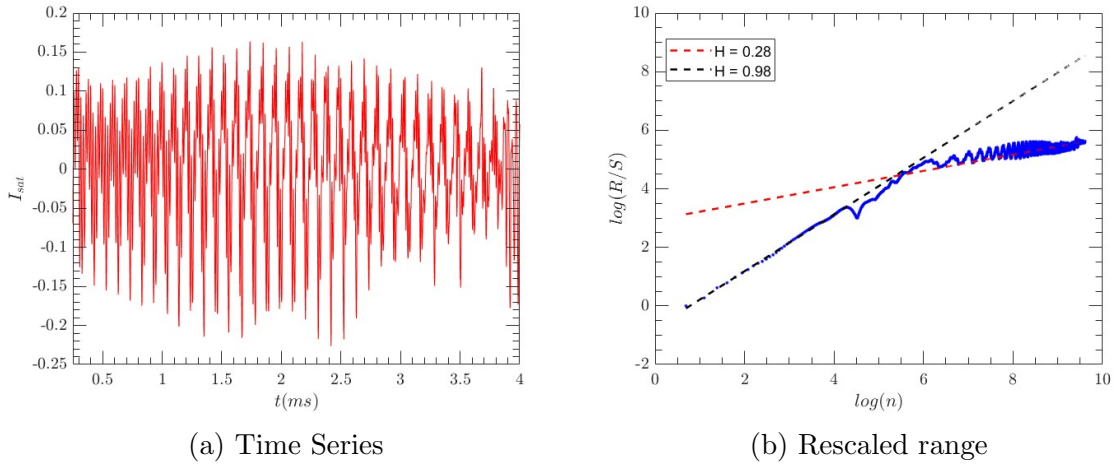
(b) Rescaled range

Figure 4.5: The rescaled range analysis for the saturation current time series at $0.1\ cm$ away from the center of the filament for the periodic segment from $0.25\ ms$ to $4\ ms$ is shown. The left panel shows the time series analyzed. The right panel shows the rescaled range plotted against the scale length on a log-log scale. A linear trend and an oscillatory trend are seen in the rescaled range and are fit by separate linear fits indicated by the dotted lines.

(a) Time Series
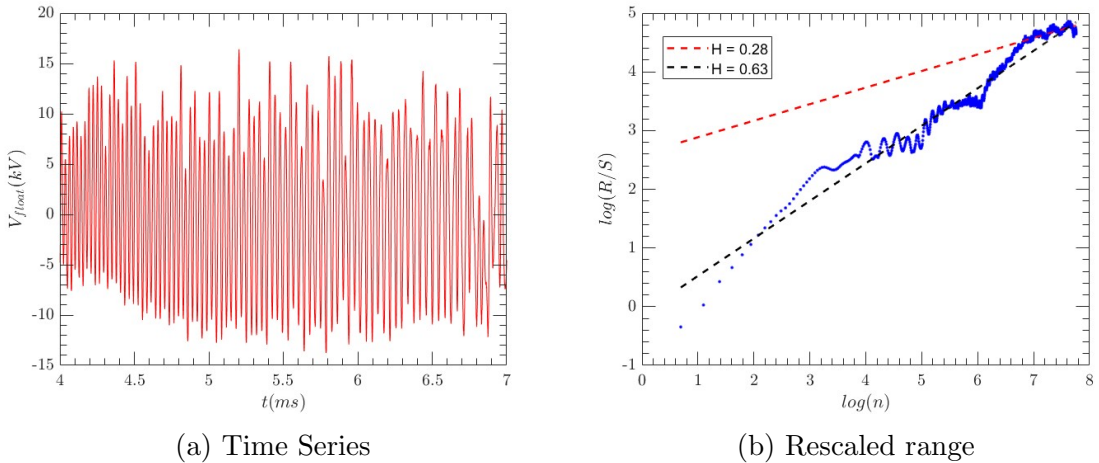
(b) Rescaled range

Figure 4.6: The rescaled range analysis for the floating voltage time series at $0.15\ cm$ away from the center of the filament for the periodic segment from $4\ ms$ to $7\ ms$ is shown. The left panel shows the time series analyzed. The right panel shows the rescaled range plotted against the scale length on a log-log scale. A linear trend and an oscillatory trend are seen in the rescaled range and are fit by separate linear fits indicated by the dotted lines.

(a) Time Series
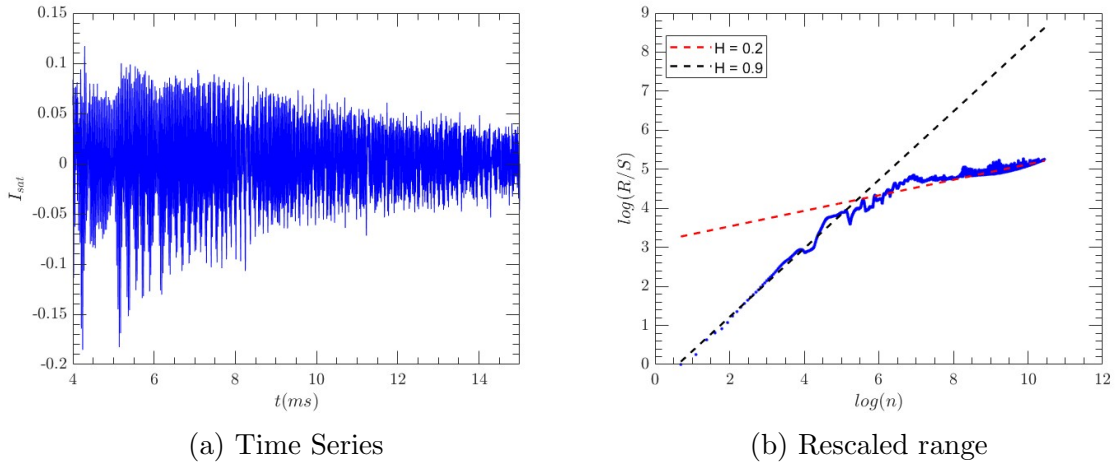
(b) Rescaled range

Figure 4.7: The rescaled range analysis for the saturation current time series at 0.1 cm away from the center of the filament for the chaotic segment from 4 ms to 15 ms is shown. The left panel shows the time series analyzed. The right panel shows the rescaled range plotted against the scale length on a log-log scale. Two different linear trends are seen in the rescaled range and are fit by separate linear fits indicated by the dotted lines.

(a) Time Series
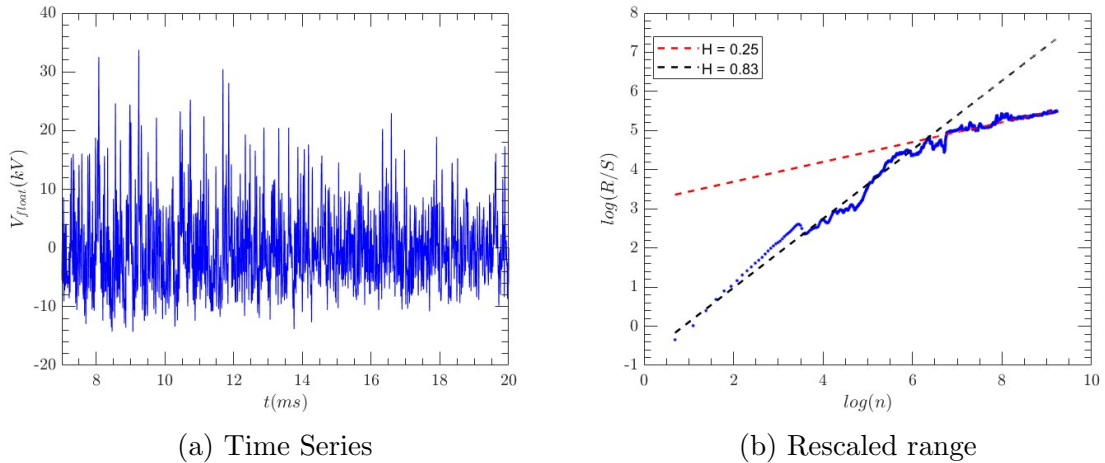
(b) Rescaled range

Figure 4.8: The rescaled range analysis of the floating voltage time series at 0.15 cm away from the center of the filament for the chaotic segment from 7 ms to 20 ms is shown. The left panel shows the time series analyzed. The right panel shows the rescaled range plotted against the scale length on a log-log scale. Two different linear trends are seen in the rescaled range and are fit by separate linear fits indicated by the dotted lines.

The floating voltage also shows similar values for both its Hurst exponents as seen
in fig.4.8b showing Hurst exponents of $H = 0.25$ and $H = 0.83$ further reinforcing
the presence of persistent and anti-persistent behaviours. As indicated through the
Lorenz map, the multiple Hurst exponents correspond to multiple time scales in the
time series. Both the voltage and current have a short time scale oscillation where
the electrons revolve around the nodes represented by the larger Hurst exponent of
the first region and a long time scale oscillation where the electrons revolve around
all the nodes represented by the smaller Hurst exponent of the second region.

The Hurst exponent analysis can also be spread over the entire 1 cm x 1 cm plane
of floating voltage data that was measured. This allows for an analysis of the change
of behaviour of the electron transport over space.

(a) H1   (b) H2
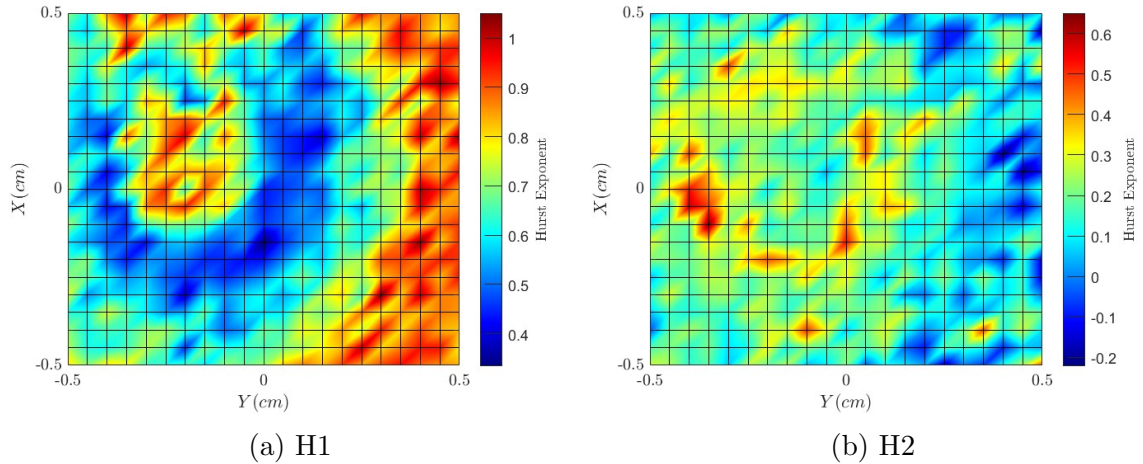
Figure 4.9: The Hurst exponents for the $1cm \times 1cm$ plane of floating voltage for
the chaotic segment from 7 ms to 20 ms is shown. The left panel shows the Hurst
exponent for the short time scale behaviour of chaotic segment while the right panel
shows the Hurst exponent of the long time scale behaviour of the chaotic segment.

The Hurst exponents for the chaotic regime of the time series seen in fig.3.2 show
two Hurst exponents over the whole region indicating the presence of two time scales
of motion. The first Hurst exponent representing the short time scale behaviour as

seen in fig.4.9a varies between values close to 1 and 0.5 showing that the short time
scale behaviour overall is mostly persistent. The Hurst exponent is closer to 1 nearer
to the center of the filament showing strong persistence near the orbit center. The
Hurst exponent drops close 0.5 showing a more random nature before settling to a
moderately high Hurst exponent indicating strong persistence. The second Hurst
exponent representing the long time scale behaviour as seen in fig.4.9b varies between
values close to 0.5 near the center and 0 further out, showing that the long time scale
behaviour overall is mostly anti-persistent. The entire surface shows a Hurst exponent
below 0.5 showing that the long time scale behaviour is completely anti-persistent.

(a) H1   (b) H2
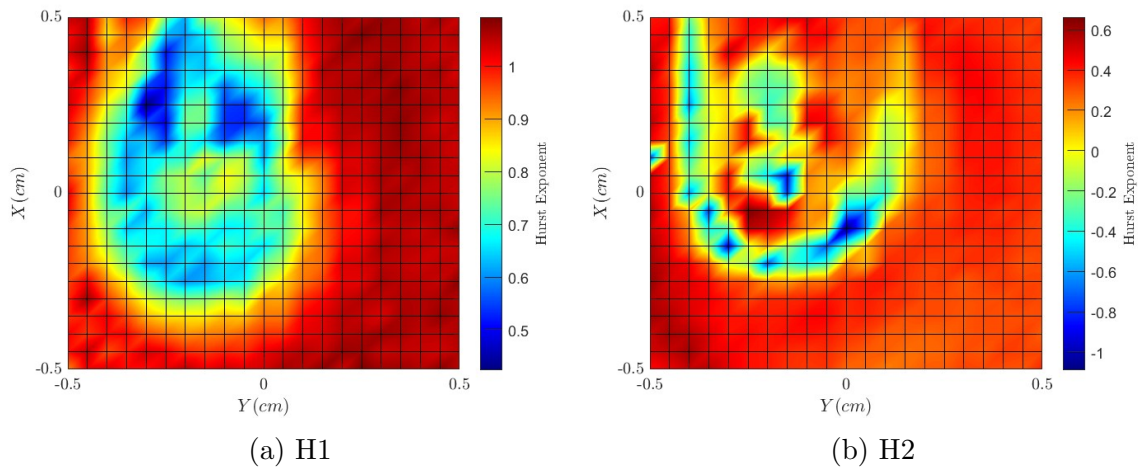
Figure 4.10: The Hurst exponents for the $1cm \times 1cm$ plane of floating voltage for
the periodic region from 0 ms to 7 ms is shown. The left panel shows the Hurst
exponent for the linear trend of the rescaled range while the right panel shows the
Hurst exponent of the oscillatory trend of the rescaled range of the periodic segment.

Fig.4.10 meanwhile, shows the Hurst exponent for the periodic region of the float-
ing voltage time series. It shows a double exponent as seen in the sine wave. The
Hurst exponent of the first segment of the rescaled range seen in fig.4.10a shows that
the Hurst exponent is close to 1 similar to a sine wave for most of the plane, save the
center of the filaments showing that the behaviour is periodic. Even there, it is still

a high Hurst exponent value showing that the behaviour is still mostly periodic. As indicated before, the floating voltage does not really show a clear second oscillatory region of rescaled range, so, the Hurst exponent shown in fig.4.10b does not give much information besides indicating that a second region does exist.

4.4 SUMMARY

Hurst exponent, introduced by Edwin Hurst, is a measure used to quantify the long term memory of a time series. The Hurst exponent is calculated using the rescaled range method.

The Hurst exponent is calculated for two common chaotic time series to show its application in practice. The Lorenz series shows two different Hurst exponents; one large and one small, indicating that it has behaviour on two time scales as well as both persistent and anti-persistent behaviour while the logistic map only shows a single Hurst exponent indicating only a single type of behaviour and time scale.

The Hurst exponent is calculated for saturation current and floating voltage to analyze the long term memory of fluctuations associated with cross-field transport. The saturation current and floating voltage time series both show a double Hurst exponent similar to the Lorenz series. This indicates that the chaotic portion of the time series has both a short time scale behaviour as well as a long time scale behaviour. Further, the short time scale behaviour has a large Hurst exponent indicating persistence in its behaviour while the long time scale behaviour has a low Hurst exponent indicating anti-persistence in its behaviour.

CHAPTER 5.

NON-LINEAR TIME SERIES ANALYSIS: LYAPUNOV EXPONENT

The Lyapunov exponent is a widely used quantitative measure to characterize deterministic chaos[55–58]. Lyapunov exponents have been used in many fields such as medicine[59, 60], naval engineering[61], fault detection[62], fluid dynamics[63], machine learning[64, 65] and more to characterize dynamical systems. Lyapunov exponent quantifies the rate of divergence or convergence of two nearby trajectories in a physical system[55, 56, 65]. Through this, the exponent can be used to measure the sensitivity of a system to initial conditions[55]. An entire range of Lyapunov exponents can be defined for a physical system based on the various trajectories present, but just the Maximum Lyapunov exponent is usually enough to analyze a time series.

Calculating the Lyapunov exponent is not an easy task. For a system whose equations of motions are known, calculating the trajectories and hence, the Lyapunov exponent is simple. However, for experimental time series, the equations of motions are not usually known. Further, most time series only measure a single variable in an experiment rather than a trajectory of a particle[55]. This results in calculating Lyapunov exponent from time series more complicated as the time series needs to somehow be converted into a trajectory first. A method to calculate the Lyapunov exponent for a uniformly sampled time series was developed by Rosenstein et al[55].

5.1 METHOD

For a given uniformly sampled time series,

$$X = \{x_1, x_2, ..., x_N\}$$

a trajectory is reconstructed in phase space with phase vectors through a time-delay method defined as[55]:

$$K_i = \{x_i, x_{i+\tau}, ..., x_{i+(m-1)\tau}\}; \ i = 1, 2, ..., m$$

Here, τ is the time lag and m is the embedding dimension. So, this gives us $M = N - (m-1)\tau$ phase vectors of length m. Each phase vector defines the state of the system at some discreet time i. Rosenstein et al. suggest choosing the embedding dimension to be below Taken's theorem and choosing the time lag to be the lag when the auto correlation function drops to $1 - 1/e$ of the initial value[55]. Once the trajectory is created, for each point on the trajectory, the closest point to it is found and the distance between those is calculated as[55]:

$$d_i(0) = min\|x_i - x_j\| \tag{5.1}$$

For every pair of "neighbours", the trajectories diverge at an exponential rate controlled by the Lyapunov exponent, λ, as[55]:

$$d_i(j) = d_i(0) \exp^{\lambda(i\Delta t)} \tag{5.2}$$

Linearizing the above equation by taking logarithm on both sides gives a set of near
parallel lines for each j with a slope of λ. These lines can then be averaged as[55]:

$$y(j) = \frac{1}{\Delta t} \langle \log(d_i(j)) \rangle \tag{5.3}$$

A least squares fit can be performed on the above curve from whose slope the Maxi-
mum Lyapunov exponent can be extracted[55].

MATLAB Predictive Maintenance toolbox has a built in function

LyapunovExponent(x,f_s,m,τ) that calculates the Lyapunov exponent of the time series
x with sampling frequency f_s. τ and m are the time lag and embedding dimension
which can be given to define the phase space vectors. First, the function constructs the
phase space vector, y from the given time lag and embedding dimension (or chooses
appropriate values if not provided). Then for each point, y_i, in the phase space, the
closest point y_j is identified such that $\|y_i - y_j\|$ is minimized and $|i-j| > Mean\ Period$.
Then, for each point, i, the Lyapunov exponent is calculated as:

$$\lambda(i) = \frac{1}{(K_{max} - K_{min} + 1)dt} \sum_{K=K_{min}}^{K_{max}} \frac{1}{K} \log \left[\frac{\|y_{i+K} - y_{j+K}\|}{\|y_i - y_j\|} \right] \tag{5.4}$$

The Maximal Lyapunov exponent is then calculated by using a standard linear curve
fit to the above curve and extracted from the slope.

A negative Lyapunov exponent indicates convergence while a positive exponent
indicates divergence. Since diverging trajectories are a defining feature of chaotic
series, a positive Lyapunov exponent is a good indicator of chaos[55–58].

5.2 SYNTHETIC TIME SERIES

To see the algorithm in action, the Lyapunov exponent is calculated for a sine wave
to show convergence and Lorenz system to show divergence. Fig.5.1 shows the results

(a) Phase Space

(b) Lyapunov Exponent Fit
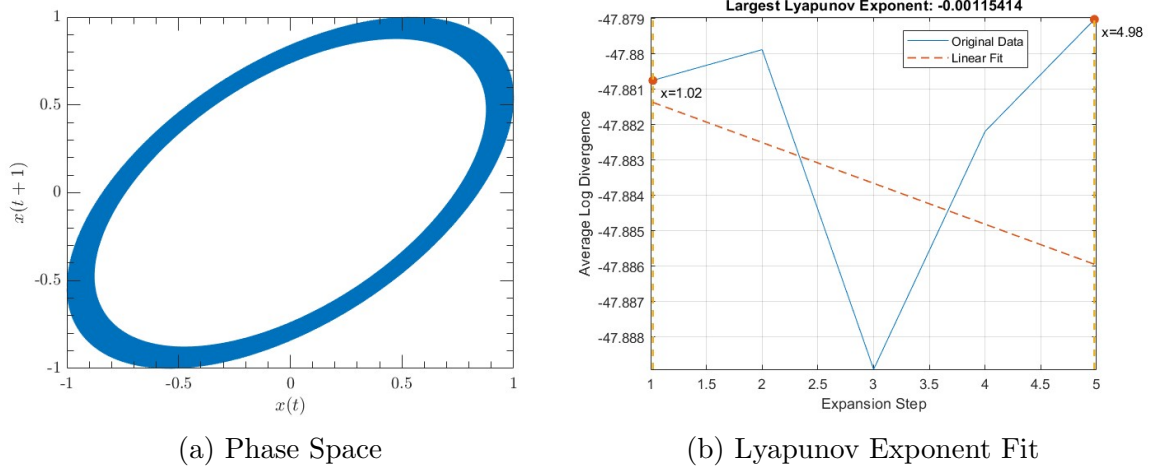
Figure 5.1: The Lyapunov exponent analysis of a sine wave is shown. The left panel
shows the trajectory of the sine wave in a phase space which has a dimension of 3
and time lag of 1. The right panel shows the linear fit to calculate the Lyapunov
exponent using the Rosenstein method.

of the algorithm for the sine wave. As expected, the phase space for a sine wave as
seen in fig.5.1a is just an ellipse. The maximum Lyapunov exponent comes out to be
-0.001 indicating converging trajectories. This is expected as every particle would
experience the exact same motion and will eventually converge as indicated visually
by the ellipse in phase space.

Fig.5.2 shows the results of the algorithm for the Lorenz system. The phase space
for the Lorenz system is the double scroll trajectory as seen in fig.5.2a . The Maximum
Lyapunov exponent is found to be 394 which shows that the trajectory is diverging
and hence confirms the chaotic nature of the Lorenz system.

Fig.5.3 shows the results of the algorithm for the Logistic series for r = 3. The
logistic series here lacks chaotic nature and this can be seen by the negative Lyapunov
exponent obtained in fig.5.3b indicating convergence of trajectories. This is further
supported by the phase space trajectory which is a simple circular trajectory resulting
in a natural convergence. Fig.5.4 shows the results of the algorithm for the Logistic

(a) Phase Space

(b) Lyapunov Exponent Fit
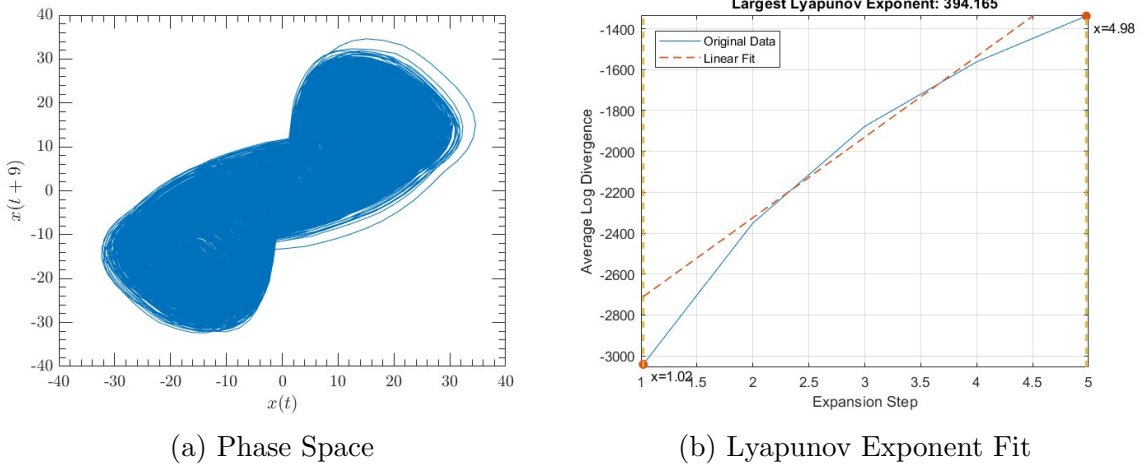
Figure 5.2: The Lyapunov exponent analysis of the Lorenz system is shown. The left panel shows the trajectory of the Lorenz system in a phase space which has a dimension of 3 and time lag of 9. The right panel shows the linear fit to calculate the Lyapunov exponent using the Rosenstein method.

(a) Phase Space

(b) Lyapunov Exponent Fit
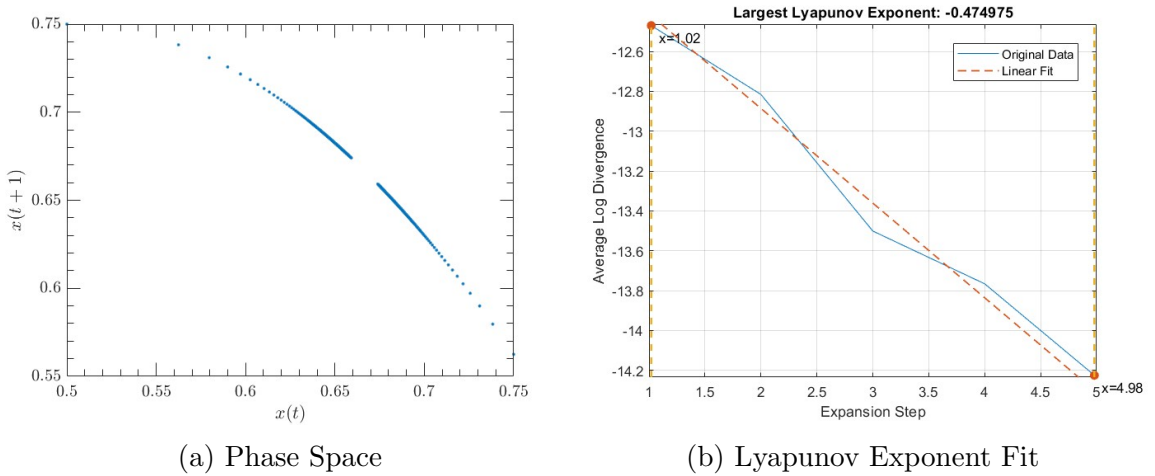
Figure 5.3: The Lyapunov exponent analysis of the logistic map for r = 3 is shown. The left panel shows the trajectory of the Logistic map in a phase space which has a dimension of 2 and time lag of 1. The right panel shows the linear fit to calculate the Lyapunov exponent using the Rosenstein method.

series for r = 3.8. The logistic series here on the other hand is chaotic in nature. This is supported by the negative Lyapunov exponent being positive as seen in fig.5.4b indicating divergence of trajectories.

(a) Phase Space

(b) Lyapunov Exponent Fit
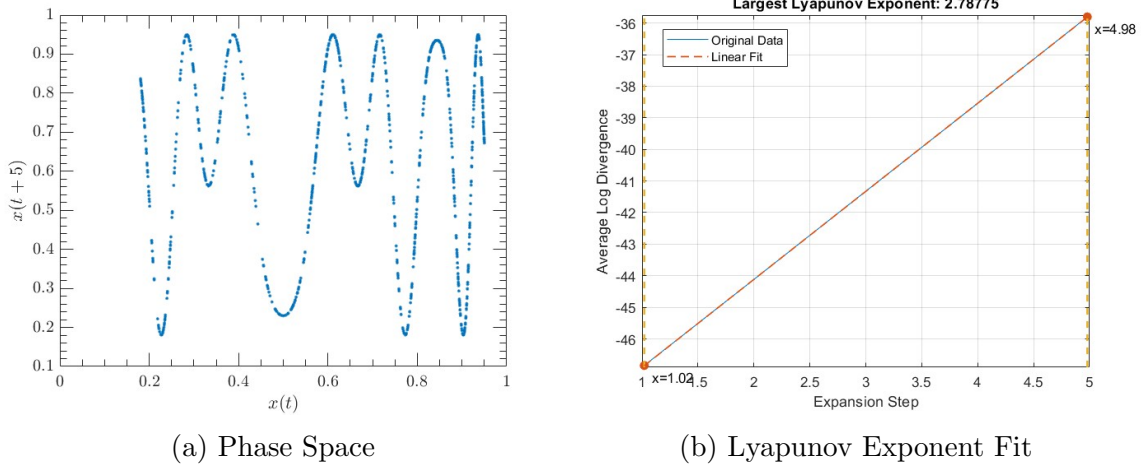
Figure 5.4: The Lyapunov exponent analysis of the logistic map for r = 3.8 is shown.
The left panel shows the trajectory of the Logistic map in a phase space which has
a dimension of 2 and time lag of 1. The right panel shows the linear fit to calculate
the Lyapunov exponent using the Rosenstein method.

5.3 COMPARISON TO HURST EXPONENT AND MACHINE LEARNING

From the previous chapter, it has been noted that Hurst exponent can also be used
as an indication of chaotic nature. This leads to the natural question of comparing
the two measures.

A Chirikov Map is used to analyze this comparison. The Chirikov map is parame-
terized by (K, p_0, x_0) exhibiting periodic, chaotic, sticky behaviour or all of the above.
The Chirikov Map is defined as[65]:

$$p_{n+1} = p_n + \frac{K}{2\pi} \sin(2\pi x_n) \tag{5.5}$$

$$x_{n+1} = x_n + p_{n+1} \tag{5.6}$$

p_0, x_0 set the initial conditons for the map while K controls the chaotic nature with

gloabal chaos occuring for $K = 0.97163540631$[65]. A set of Chirikov maps are made
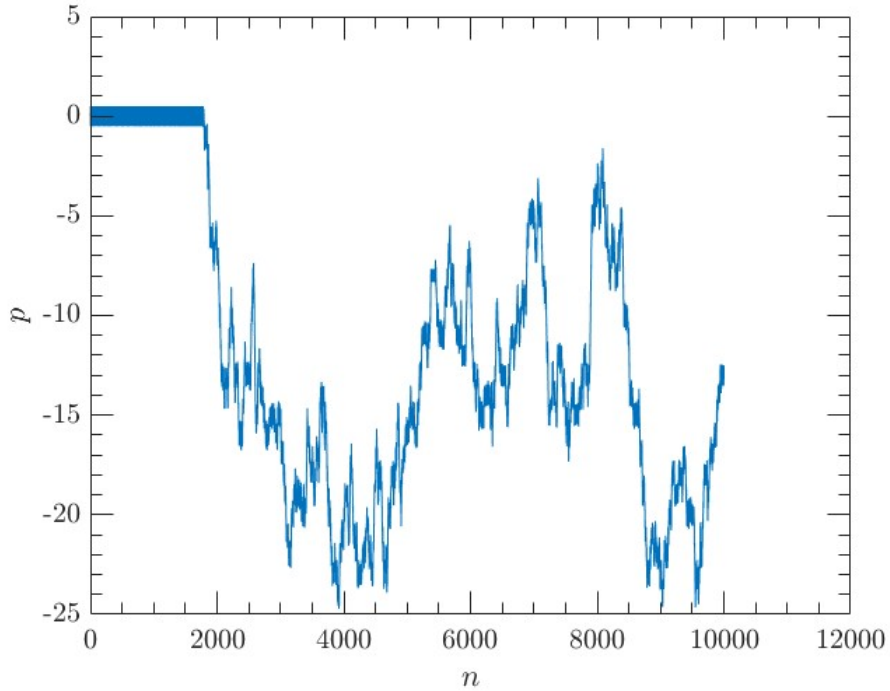
Figure 5.5: The Chirikov map for $K = 3.228259$, $x_0 = 0.2865$ and $p_0 = 0$ is shown.

by varying K and x_0 while keeping $p_0 = 0$. Then, the Lyapunox exponent and Hurst exponents are calculated for these maps giving us a surface in a $K \times x_0$ domain. As seen in fig.5.6 , Lyapunov Exponent and Hurst exponent are similarly correlated to each other for the Chirikov Map[65]. This can now be used to train a machine learning algorithm to calculate the Hurst exponent for a Chirikov Map of a given K and x_0.

Machine learning (ML) is a computational technique used to predict a certain quantity of interest by building a model based on existing data to be applied on future data to be collected[66]. In simplest possible terms, Machine Learning is a method to solve an optimization problem based on a multi-dimensional model. A data set of the system under consideration containing a set of input variables characterizing the

(a) Lyapunov Exponent
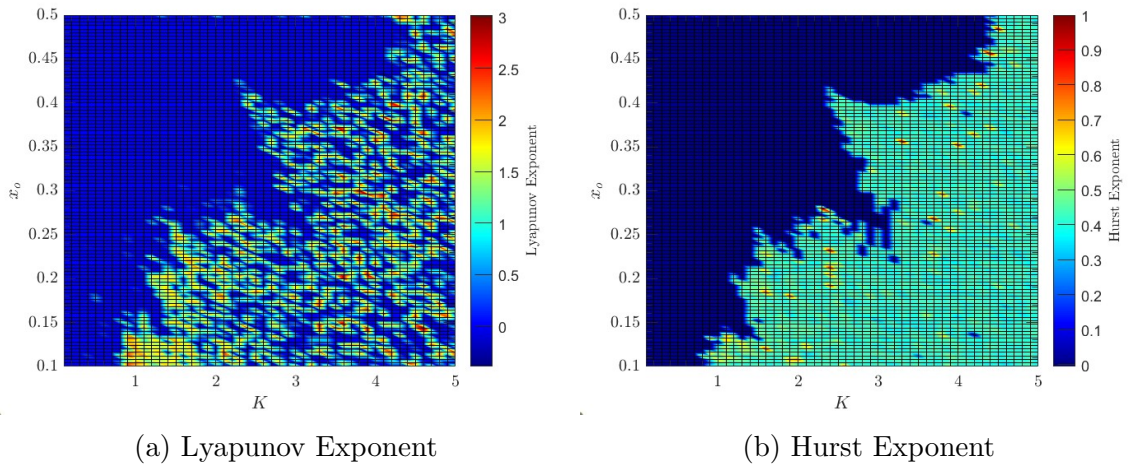
(b) Hurst Exponent

Figure 5.6: The comparison between the Lyapunov exponent on the left and the Hurst exponent on the right is shown for the Chirikov map in a $K \times x_0$ domain with $p_0 = 0$.

state of the system, called the features of a system, and the output variables defining the quantity of interest, called labels of a system, is built called the training data[66]. This is fed to ML algorithms which over many iterations build a set of functions that map each feature of the system to its respective label. The set of these mapping functions is called a hypothesis space[66]. Armed with this hypothesis space, the machine learning algorithm can then be used to predict labels for features in new data sets from experiments. There are many different algorithms to perform machine learning such as deep learning, neural networks, and more[66]. For our purposes, a k-nearest neighbours algorithm will be used.

Nearest Neighbour methods is a collection of various methods used to solve regression problems involving numeric labels,i.e, $y \in \mathbb{R}$, by constructing a hypothesis space[66]. The most commonly used type of space and the one used for the analysis in this thesis is Euclidean space with the vector distance, $\|x - x'\|$ also belonging to

the same space[66]. So, consider a given data set,

$$D = \{x_i, y_i\} \tag{5.7}$$

where x_i are the features and y_i are its respective labels. Further, let X and Y be
the space containing all the features and labels of the data set respectively. Then,
a hypothesis space is built made of maps $h(x) : X \longrightarrow Y$ where, $h(x)$ for a feature
x, only depends on the labels of the k nearest neighbours to that feature as defined
by the euclidean distance to those neighbours[66]. Hence, this method is usually
known as k-nearest neighbours method. The downside to this method is that it is
very dependant on the training data set given to it[66]. For a data with new features,
the algorithm needs to be trained again using those new features. This downside is
not a major problem for our purposes as we are only analyzing a single model and
experiment. For the algorithm used in this thesis, only a single nearest neighbour is
used[65]. MATLAB Statistical and Machine Learning toolbox has a built-in function
fitcknn(labels,features) that takes in the labels and features of a system and builds
a k-nearest neighbours model object that can then be passed to *predict(model,data)*
along with the data to predict the labels for the features seen in experimental data.

To show the k-nearest neighbours method in action, it is applied to the Chirikov
map chaotic exponents to show how it predicts Hurst exponents based on Lyapunov
exponents. For training the machine learning program, the Lyapunov and Hurst
exponent surfaces previously made will be used[65]. The input variables of K, x_0
and the Lyapunov exponent are fed to the program with the Hurst exponents being
the labels to be predicted[65]. This allows the program to build a model that can
now predict Hurst exponents of a Chirikov map given the K, x_0 and the Lyapunov
exponent values. To test our model, the Lyapunov exponents used in the training set

are fed into the model to see if it can predict the Hurst exponents correctly. It can

seen from fig.5.7 , that it does predict the Hurst exponents correctly.
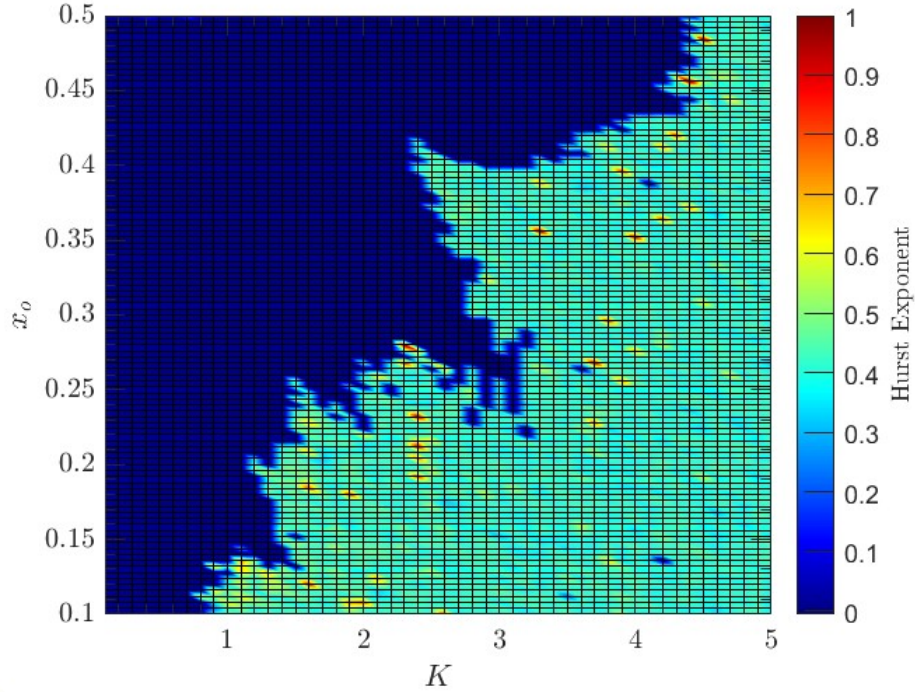
Figure 5.7: The Hurst exponent predicted by the machine learning model when fed
the Lyapunov exponents from the training set.

5.4 EXPERIMENTAL TIME SERIES

Now, the Lyapunov exponent is calculated for the experimental data from the

electron transport experiment. Further, a comparison is also made the the Hurst

exponent results from the previous chapter.

Fig.5.8a shows the Lyapunov exponent for the entire 1 cm x 1 cm surface for the

chaotic section of the time series. The entire surface has a high Lyapunov exponent

showing that the entire region is chaotic in nature. The regions closer to the filament

also have a higher Lyapunov exponent as compared to regions farther out indicating

that the chaotic nature reduces as the distance from the filament increases. Moreover,

(a) Chaotic section   (b) Periodic section
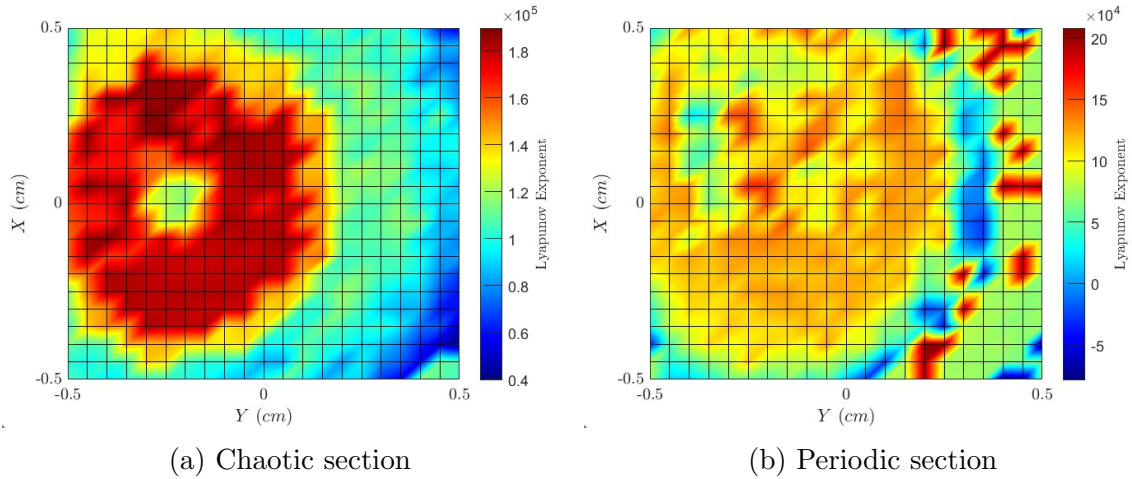
Figure 5.8: The Lyapunov exponents for the $1cm \times 1cm$ plane of the Floating voltage time series experimental data is shown. The left panel shows the Lyapunov exponents of the chaotic segment of the time series which ranges from $7 \ ms$ to $20 \ ms$ while the right panel shows the Lyapunov exponents of the periodic segment of the time series which ranges from $0 \ ms$ to $7 \ ms$

the actual location of the filament also shows a low Lyapunov exponent which is expected as there is not much transport happening exactly at the filament.

Comparing the surface of Lyapunov exponents in fig.5.8a to the Hurst exponents in fig.4.9, a remarkable similarity can be seen. Though they are similar, they are inverted in that where the Lyapunov exponent is higher, the Hurst exponent is lower and vice versa. So, when the time series is more chaotic, it is less persistent. This is even more apparent in fig.5.9 which shows the comparison between the two exponents in a radial direction. It can be seen that while the hurst exponent starts low and increases further out from the filament, the Lyapunov exponent starts out higher and drops lower further away from the filament.

To further confirm our results, machine learning is used to see if the results can be replicated. Shi, Pace et al. modeled the electric potential around filamentary heat
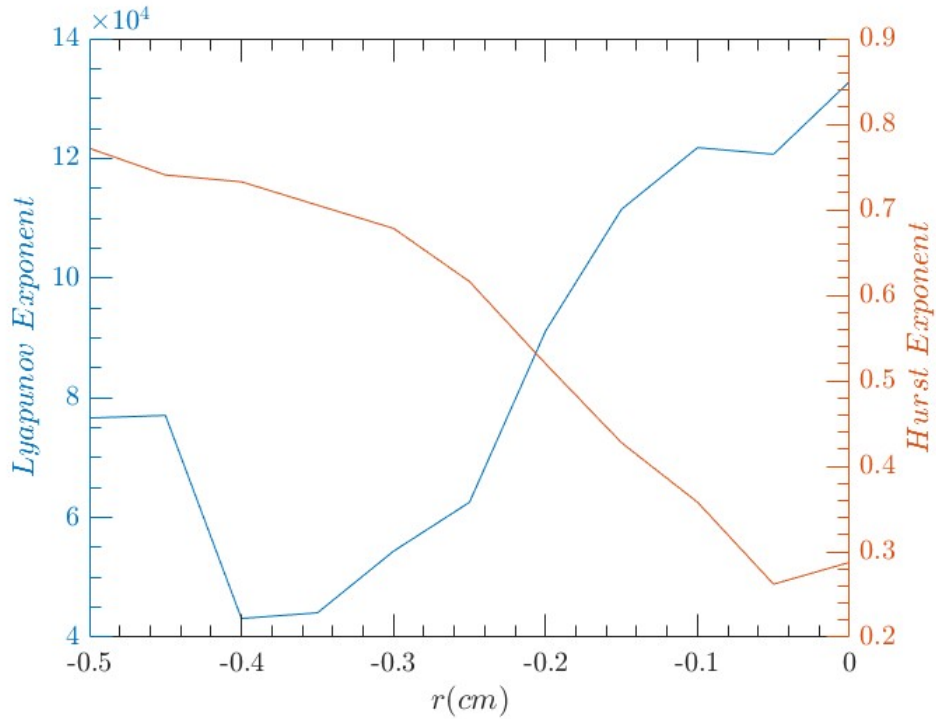
Figure 5.9: The comparison between the Lyapunov exponents and the Hurst exponents of the floating voltage time series in a radial direction from 0 cm to -0.5 cm along the y-direction and at 0 cm along the x-direction for the chaotic segment of the time series which ranges from 7 ms to 20 ms is shown.

sources as discussed in Chapter 1 and is given below[5]:

$$\Phi(r, \theta, t) = Re\left[A_1 J_1(k_1 r)e^{i\theta}e^{-i\omega t}e^{-\alpha r}\right] + Akr^2 \tag{5.8}$$

The drift waves generated from a single temperature filament only show the first mode and the global mode. This can be used to create a model of our time series during the periodic section. Further, the CH Planes in fig.3.5 and fig.3.7 can be used to find and add in the relevant noise levels to more closely match the model to our data. The resulting Shi-Pace model is seen in fig.5.10 . This model can then be used to calculate the Lyapunov and Hurst exponents, seen in fig.5.11, to train a machine
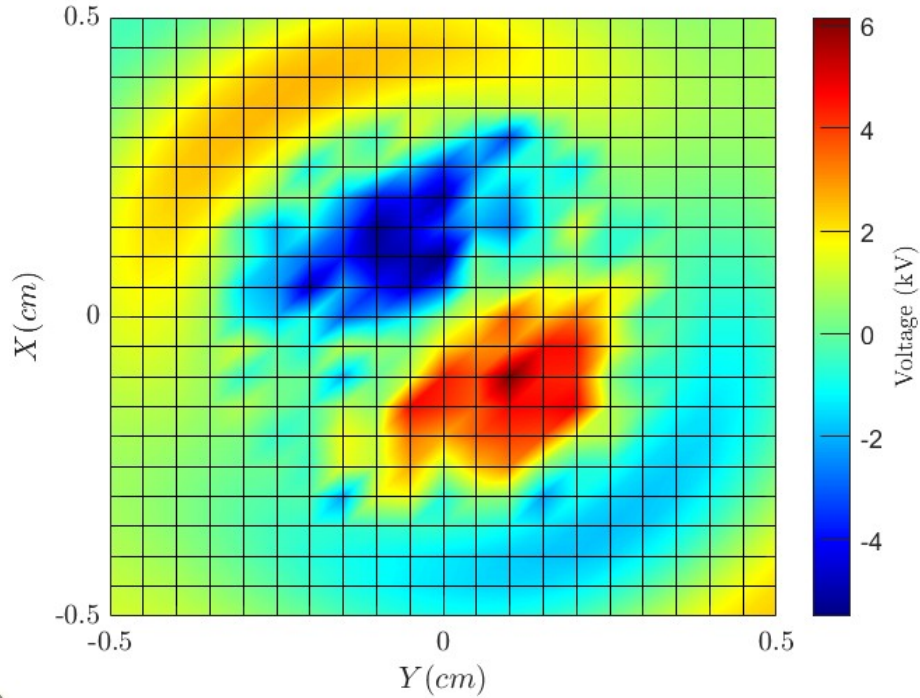
Figure 5.10: The Shi-Pace model with the appropriate noise scaling added in that is
used for building the training data set is shown.

learning algorithm. As seen in fig.5.11, the Lyapunov exponent and Hurst exponent
of the Shi-Pace model shows a clear anti-correlation between them like in our data.
This acts as the first check to show that our experimental results are accurate.

Now, a nearest neighbours machine learning algorithm is trained using the Lya-
punov exponent and Hurst exponent from the Shi-Pace model similar to the Chirikov
map from earlier to relate the Lyapunov exponent to the Hurst exponent. Once
the algorithm is trained, it is applied to the Lyapunov exponent acquired from our
data. As seen from fig.5.12b, the Hurst exponent predicted by the algorithm has low
Hurst exponent near the center of the filament while it is much higher further away.
Comparing the result produced by the machine learning algorithm to the results ac-
quired from the data, it can be seen from fig.5.12 that while the machine learning

(a) Hurst Exponent   (b) Lyapunov Exponent
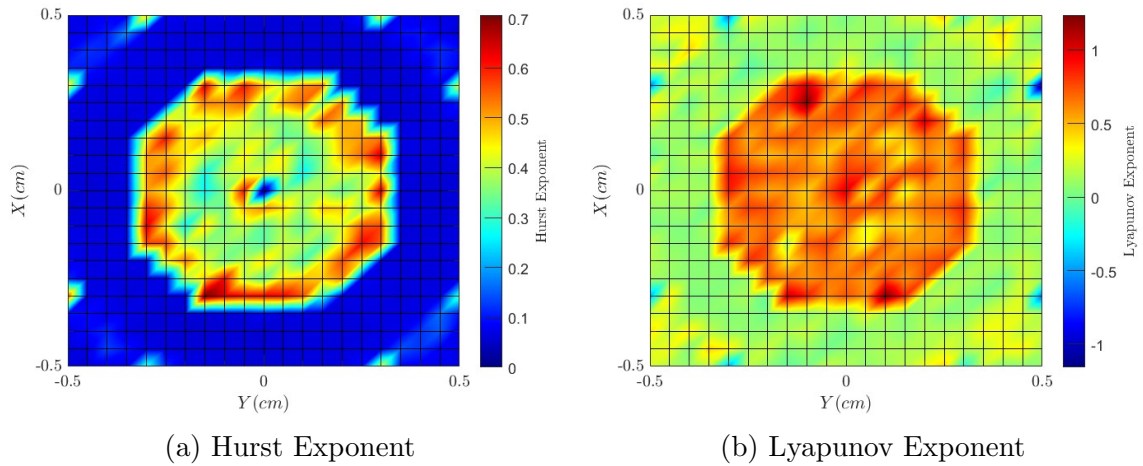
Figure 5.11: The comparison between the Hurst exponents on the left and the Lyapunov exponent on the right for a $1cm \times 1cm$ plane of the Shi-Pace potential model is shown.

results are extreme, they match with the experimental results. They both show a low Hurst exponent near the filaments while the region outside the filaments shows a high Hurst exponent. This shows that even the machine learning algorithm predicts strong anti-correlation between Lyapunov and Hurst exponents. This is expected as the strong periodic nature of the drift waves leads to low Lyapunov exponent while the persistence of the periodic oscillations of the drift waves leads to higher Hurst exponent. However, some radial variation in the chaotic exponents can be seen. This is also expected due to the temperature gradient of the background plasma resulting in a higher noise level near the filament increasing the Lyapunov exponent due to the noise adding more chaotic elements closer to the filament and lower Hurst exponent due to more anti-persistence near the filament. This is the final confirmation showing the validity of the experimental results.

(a) Hurst Exponent from Data

(b) Hurst Exponent from ML
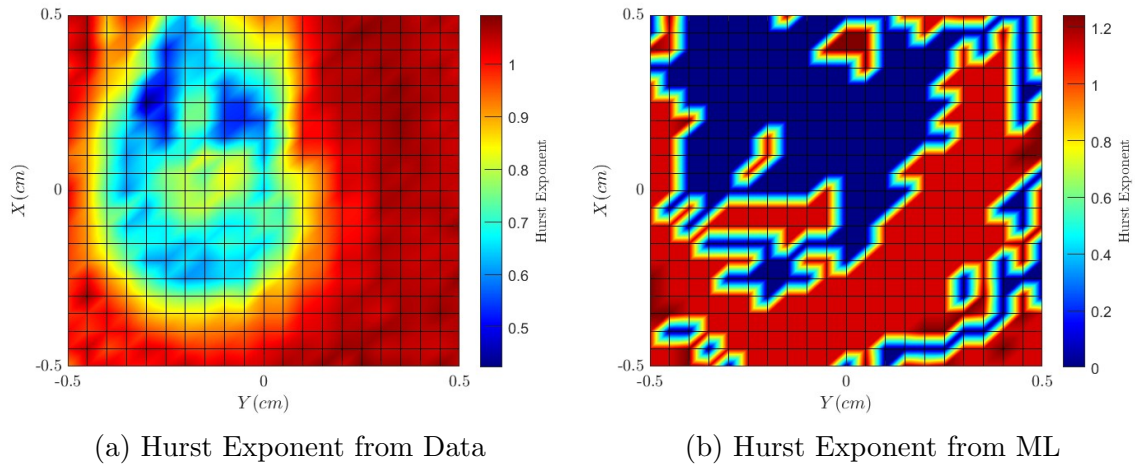
Figure 5.12: The comparison between the Hurst exponent acquired from the machine learning algorithm and the Hurst exponent acquired from data for the periodic segment of the $1cm \times 1cm$ plane of the floating voltage time series experimental data is shown. The left panel shows the Hurst exponent acquired by applying rescaled range method to the periodic segment of the experimental time series. The right panel shows the Hurst exponents acquired by applying Machine Learning to the Lyapunov exponent of the periodic segment of the experimental time series.

5.5 SUMMARY

Lyapunov exponent is a widely used measure to quantify the chaotic nature of a system. Lyapunov exponent is generally calculated from particle trajectories defined by equations of motion. However, this is difficult to perform with experimental time series as the equations of motion are not usually known and the quantities under investigation may not even be able to define such equations. Rosenstein et al. developed a method to calculate Lyapunov exponents for time series by building trajectories in a phase space created by time-delayed series.

This method is used to analyze various synthetic time series: sine wave, Lorenz system, and Logistic map as well as the experimental time series. The sine wave and the Logistic map for $r = 3$ show negative Lyapunov exponents indicating periodic nature while the Lorenz system and the Logistic map for $r = 3.8$ show a positive Lyapunov

exponent indicating chaotic nature.

Further, Machine Learning is also used to show the relationship between Lyapunov and Hurst exponents. A k-nearest neighbours algorithm is trained on the Lyapunov and Hurst exponents of Chirikov map to show this in action. Finally, the Lyapunov exponent is calculated for the experimental data from the electron heat transport experiment. The Lyapunov exponent is calculated for the $1cm \times 1cm$ plane of floating voltage and comparing it to the Hurst exponent, an anti-correlation between them is seen. To further confirm this, a k-nearest neighbours machine learning algorithm to predict Hurst exponents from Lyapunov exponents is trained using the Lyapunov and Hurst exponents from the Shi-Pace potential model which models the electron heat transport. This model is then fed the Lyapunov exponent based on the experimental data and it is seen that it also predicts anti-correlation between Lyapunov and Hurst exponents. This confirms our experimental results.

Therefore, Lyapunov exponent is shown to be a good measure of chaotic nature and is compared to Hurst exponent. These results are used to analyze and confirm our experimental results.

CHAPTER 6.

Summary and Future Work

Understanding fluctuations from temperature filaments in plasmas is an important avenue for research as these structures are common in edge regions of magnetically confined plasmas. Through the course of this thesis, an analysis of non-linear time series of fluctuations from a plasma experiment designed to explore transport from filamentary structures was shown. To do this, three methods to analyze non-linear time series are explored: CH-Plane method, Hurst exponent and Lyapunov exponent.

Chapter 2 introduced the CH-Plane methodology formulated by Rosso et al[21]. It is a method to determine the nature of a time series as periodic, chaotic, stochastic or noise by plotting the complexity of the time series against its complexity and analyzing its location on the resulting complexity-entropy plane or CH-Plane. To calculate entropy and complexity, the probability of occurrence of various states of a system need to be known. Experimental data however is usually collected as discreet time series rather than probability densities. Here, a method introduced by Bandt and Pompe is used which allows a probability density to be defined for any arbitrary time series through defining amplitude permutations of smaller embedded segments of the time series as its states[20]. With the probability density, Shannon Entropy is used as the entropy and Jensen-Shannon Divergence is used as the complexity. Further, an upper and lower bounds are added to the complexity values. All of this is used to build the CH-Plane which can be used to analyze non-linear time series to determine their nature.

Chapter 3 introduces the plasma experiment under observation and analyzes the fluctuations time series acquired from that experiment using the CH-Plane method. The plasma experiment was performed in the Large Plasma Device at UCLA by Scott Karbaschewski and Dr. Van Compernoll[36]. The experiment used a ohmically heated crystal cathode to generate a long high temperature filament in a cold plasma background. Then, a Langmuir probe was used to record fluctuations in saturation current and floating voltage arising from the filament in a $1cm \times 1cm$ plane around the filament. The current and voltage time series acquired from the plasma experiment is then analyzed using the previously introduced CH Planes. It is shown that the fluctuations start with periodic nature before transitioning to chaotic nature. It is also shown that the chaotic nature drops off radially from the filament following the density and temperature gradient. Through this chapter, the application of CH-Planes to experimental data is shown by analyzing fluctuations acquired from a plasma experiment.

Chapter 4 introduced Hurst exponents, a common quantifier for memory of a time series. Hurst exponent is a measure used to quantify if a time series will continue its current increasing or decreasing trend in amplitude, persistence, or switch to the opposing trend in the future, anti-persistence. It was found that chaotic series have multiple Hurst exponents with each exponent corresponding to the various time scales of behaviour[50]. This knowledge was used to analyze the current and voltage fluctuation from the plasma experiment. It was shown that fluctuations start with periodic nature and then switch to chaotic nature confirming the CH-Plane analysis. Further, by calculating the Hurst exponent for the entire plane of data, it was shown that the chaotic section of the time series shows persistence for the short-time scale behaviour while the long time scale behaviour is persistent. The periodic section was shown to be persistent in nature. So, through this chapter, an analysis of memory

was added onto the knowledge gained from the CH-Plane analysis to give a better classification of the chaotic and periodic sections of the fluctuations from filamentary structures in plasma.

Chapter 5 introduced the Lyapunov exponent, a common measure to identify the chaotic nature of time series. Lyapunov exponent quantifies the degree of separation of two particles in a system that start nearby as the system evolves. A positive Lyapunov exponent indicates chaos while a negative exponent indicates periodic nature. This however requires knowledge of particle motion which is not always feasible in experimental data resulting in a need for a method to calculate Lyapunov exponents for arbitrary time series. To this end, Rosenstein et al., developed a method that used phase-space trajectories in a time-delayed phase space constructed from the time series to calculate the Lyapunov exponent[55]. Using this method, it is shown that the current and voltage fluctuations from the plasma experiment start with periodic nature before shifting to a chaotic nature matching the results acquired from CH-Plane and Hurst exponent analysis. Further, Machine Learning algorithm is used to relate Lyapunov exponents to Hurst exponents. A k-nearest neighbours machine learning algorithm is trained on the Shi-Pace drift wave model to predict the Hurst exponent when provided the Lyapunov exponent. This then applied to the Lyapunov exponent calculated from the fluctuation data from the plasma experiment and it was shown that the machine learning algorithm prediction of the Hurst exponent matches the results acquired earlier in the thesis. Through this, the application of Lyapunov exponents to non-linear time series analysis is shown as well as the use of Machine Learning to analyze chaos in time series.

Through these various methods of analysis of non-linear time series, it has been shown that fluctuations from filament-like structures in plasma start with periodic nature before developing chaotic features. However, filament-like structures appear

in groups in general unlike the plasma experiment described in this thesis which only analyzed a single filament. The fluctuations from multiple filaments is more complicated due to interactions between particle transports from multiple filaments resulting in higher mode drift waves as well as vortices and turbulence. Plasma experiments have been conducted on multiple heat filaments such as the ones by Dr. Scott Karbashewski and Dr. Sydora[24, 36, 39]. Applying the methods described in this thesis to the fluctuation results from those experiments could provide great insight into the transport behaviour due to multiple filaments and is a great avenue for future research.

This thesis acts as a record of non-linear time series analysis applied to plasma experiments. Through the course of this thesis, a variety of non-linear time series analysis methods are presented and applied to a plasma experiment.

References

[1] F. F. Chen, *Introduction to Plasma Physics and Controlled Fusion*, Vol. 1 (Springer, 1984).

[2] S. Karbashewski, R. D. Sydora, B. Van Compernolle, and M. J. Poulos, Phys. Rev. E **98**, 051202 (2018).

[3] G. Serianni, M. Agostini, V. Antoni, R. Cavazzana, E. Martines, F. Sattin, P. Scarin, E. Spada, M. Spolaore, N. Vianello, *et al.*, Plasma Physics and Controlled Fusion **49**, B267 (2007).

[4] A. T. Burke, J. E. Maggs, and G. J. Morales, Physics of Plasmas **7**, 544 (2000), https://doi.org/10.1063/1.873840 .

[5] M. Shi, D. Pace, G. Morales, J. Maggs, and T. Carter, Physics of Plasmas **16**, 062306 (2009).

[6] H. Wold, *A study in the Analysis of Stationary Time Series*, Ph.D. thesis, Almqvist & Wiksell (1938).

[7] S. Bittanti and P. Colaneri, in *Control and Dynamic Systems*, Vol. 78 (Elsevier, 1996) pp. 313–339.

[8] Z. Liu, Mathematical Problems in Engineering **2010**, 720190 (2010).

[9] J. Theiler, JOSA A **7**, 1055 (1990).

[10] R. Friedrich, J. Peinke, M. Sahimi, and M. R. R. Tabar, Physics Reports **506**, 87 (2011).

[11] M. Dämmig and F. Mitschke, Physics Letters A **178**, 385 (1993).

[12] A. Provenzale, L. A. Smith, R. Vio, and G. Murante, Physica D: Nonlinear Phenomena **58**, 31 (1992).

[13] L. Zunino, M. C. Soriano, and O. A. Rosso, Phys. Rev. E **86**, 046210 (2012).

[14] A. Osborne, A. Kirwan Jr, A. Provenzale, and L. Bergamasco, Physica D: Nonlinear Phenomena **23**, 75 (1986).

[15] R. Vio, S. Cristiani, O. Lessi, and A. Provenzale, The Astrophysical Journal **391**, 518 (1992).

[16] A. R. Osborne and A. Provenzale, Physica D: Nonlinear Phenomena **35**, 357 (1989).

[17] A. Provenzale, A. t. R. Osborne, and R. Soj, Physica D: Nonlinear Phenomena **47**, 361 (1991).

[18] D. Mandic, M. Chen, T. Gautama, M. Van Hulle, and A. Constantinides, Proceedings of the Royal Society A: Mathematical, Physical and Engineering Sciences **464**, 1141 (2008).

[19] J. Fan and Q. Yao, *Nonlinear Time Series: Nonparametric and Parametric Methods*, Vol. 20 (Springer, 2003).

[20] C. Bandt and B. Pompe, Physical Review Letters **88**, 174102 (2002).

[21] M. Martin, A. Plastino, and O. Rosso, Physica A: Statistical Mechanics and its Applications **369**, 439 (2006).

[22] C. Anteneodo and A. R. Plastino, Physics Letters A **223**, 348 (1996).

[23] J. Maggs and G. Morales, Plasma Physics and Controlled Fusion **55**, 085015 (2013).

[24] S. Karbashewski, R. Sydora, B. Van Compernolle, T. Simala-Grant, and M. Poulos, Physics of Plasmas **29**, 112309 (2022).

[25] F. Montani and O. A. Rosso, Entropy **16**, 4677 (2014).

[26] R. Baravalle, O. A. Rosso, and F. Montani, Physica A: Statistical Mechanics and its Applications **511**, 27 (2018).

[27] W. Legnani, F. Traversaro, F. O. Redelico, L. J. Cymberknop, R. L. Armentano, and O. A. Rosso, Chaos: An Interdisciplinary Journal of Nonlinear Science **28**, 075518 (2018).

[28] L. Zunino, M. Zanin, B. M. Tabak, D. G. Pérez, and O. A. Rosso, Physica A: Statistical Mechanics and its Applications **389**, 1891 (2010).

[29] S. López-Rosa, I. Toranzo, P. Sánchez-Moreno, and J. Dehesa, Journal of Mathematical Physics **54**, 052109 (2013).

[30] L. Zunino and H. V. Ribeiro, Chaos, Solitons & Fractals **91**, 679 (2016).

[31] O. A. Rosso, H. Larrondo, M. T. Martin, A. Plastino, and M. A. Fuentes, Physical Review Letters **99**, 154102 (2007).

[32] H. Xiong, P. Shang, J. He, and Y. Zhang, Nonlinear Dynamics **100**, 1673 (2020).

[33] T. E. Duncan, Y. Hu, and B. Pasik-Duncan, SIAM Journal on Control and Optimization **38**, 582 (2000).

[34] A. M. Chrisment and M.-C. Firpo, Physica A: Statistical Mechanics and its Applications **460**, 162 (2016).

[35] P. J. Weck, D. A. Schaffner, M. R. Brown, and R. T. Wicks, Physical Review E **91**, 023101 (2015).

[36] R. D. Sydora, S. Karbashewski, B. Van Compernolle, M. J. Poulos, and J. Loughran, Journal of Plasma Physics **85**, 905850612 (2019).

[37] W. Gekelman, P. Pribyl, Z. Lucky, M. Drandell, D. Leneman, J. Maggs, S. Vincena, B. Van Compernolle, S. Tripathi, G. Morales, *et al.*, Review of Scientific Instruments **87**, 025105 (2016).

[38] R. L. Merlino, American Journal of Physics **75**, 1078 (2007).

[39] S. Karbashewski, R. Sydora, B. Van Compernolle, and M. Poulos, Physics of Plasmas **28**, 092112 (2021).

[40] R. F. Ceballos and F. F. Largo, Imperial Journal of Interdisciplinary Research **3**, 424 (2017).

[41] H. E. Hurst, Transactions of the American society of civil engineers **116**, 770 (1951).

[42] G. Wang, G. Antar, and P. Devynck, Physics of Plasmas **7**, 1181 (2000).

[43] M. Gilmore, C. Yu, T. Rhodes, and W. Peebles, Physics of Plasmas **9**, 1312 (2002).

[44] C. L. Franzke, S. M. Osprey, P. Davini, and N. W. Watkins, Scientific Reports **5**, 1 (2015).

[45] S. F. Wang, R. Mosdorf, and M. Shoji, International Journal of Heat and Mass Transfer **46**, 1519 (2003).

[46] L. Luo, Y. Yan, P. Xie, J. Sun, Y. Xu, and J. Yuan, Chemical Engineering Journal **181**, 570 (2012).

[47] J. Mielniczuk and P. Wojdyłło, Computational Statistics & Data analysis **51**, 4510 (2007).

[48] K. H. Hamed, Water Resources Research **43**, 797–809 (2007).

[49] R. Bryce and K. Sprague, Scientific Reports **2**, 315 (2012).

[50] V. Suyal, A. Prasad, and H. P. Singh, Solar Physics **260**, 441 (2009).

[51] Y. Zeng and S. N. Singh, Dynamics and Control **7**, 143 (1997).

[52] S.-K. Yang, C.-L. Chen, and H.-T. Yau, Chaos, Solitons & Fractals **13**, 767 (2002).

[53] E. N. Lorenz, Journal of Atmospheric Sciences **20**, 130 (1963).

[54] S. Phatak and S. S. Rao, Physical Review E **51**, 3670 (1995).

[55] M. T. Rosenstein, J. J. Collins, and C. J. De Luca, Physica D: Nonlinear Phenomena **65**, 117 (1993).

[56] U. Parlitz, Estimating lyapunov exponents from time series, in *Chaos Detection and Predictability* (Springer, 2016) pp. 1–34.

[57] A. Wolf, J. B. Swift, H. L. Swinney, and J. A. Vastano, Physica D: Nonlinear Phenomena **16**, 285 (1985).

[58] H. Kantz, Physics Letters A **185**, 77 (1994).

[59] B. Swiderski, S. Osowski, and A. Rysz, in *Proceedings of the 2005 European Conference on Circuit Theory and Design, 2005.*, Vol. 2 (IEEE, 2005) pp. II–153.

[60] A. Giovanni, M. Ouaknine, and J.-M. Triglia, Journal of Voice **13**, 341 (1999).

[61] L. S. McCue and A. W. Troesch, Use of lyapunov exponents to predict chaotic vessel motions, in *Contemporary Ideas on Ship Stability and Capsizing in Waves* (Springer, 2011) pp. 415–432.

[62] W. Caesarendra, B. Kosasih, K. Tieu, and C. A. Moodie, in *2013 IEEE/ASME International Conference on Advanced Intelligent Mechatronics* (IEEE, 2013) pp. 1713–1718.

[63] T. Peacock and G. Haller, Physics Today **66**, 41 (2013).

[64] N. F. Güler, E. D. Übeyli, and I. Güler, Expert Systems with Applications **29**, 506 (2005).

[65] M. Tarnopolski, Physica A: Statistical Mechanics and its Applications **490**, 834 (2018).

[66] A. Jung, *Machine learning: The Basics* (Springer Nature, 2022).